REPORT DOCUMENTATION PAGE

Form Approved
OMB No. 0704-0188

The public reporting burden for this collection of information is estimated to average 1 hour per response, including the time for reviewing instructions, searching existing data sources, gathering and maintaining the data needed, and completing and reviewing the collection of information. Send comments regarding this burden estimate or any other aspect of this collection of information, including suggestions for reducing the burden, to Department of Defense, Washington Headquarters Services, Directorate for Information Operations and Reports (0704-0188), 1215 Jefferson Davis Highway, Suite 1204, Arlington, VA 22202-4302. Respondents should be aware that notwithstanding any other provision of law, no person shall be subject to any penalty for failing to comply with a collection of information if it does not display a currently valid OMB control number.
PLEASE DO NOT RETURN YOUR FORM TO THE ABOVE ADDRESS.

1. REPORT DATE *(DD-MM-YYYY)*	2. REPORT TYPE	3. DATES COVERED *(From - To)*
02-06-2006	Final	Oct 2004--Mar 2006

4. TITLE AND SUBTITLE

Time-Domain Simulations of Problems in Ocean Acoustics

5a. CONTRACT NUMBER

5b. GRANT NUMBER

N00014-05-0101

5c. PROGRAM ELEMENT NUMBER

6. AUTHOR(S)

John B. Schneider

5d. PROJECT NUMBER

5e. TASK NUMBER

5f. WORK UNIT NUMBER

7. PERFORMING ORGANIZATION NAME(S) AND ADDRESS(ES)

Washington State University
P.O. Box 642752
Pullman, WA 99164-2752

8. PERFORMING ORGANIZATION REPORT NUMBER

9. SPONSORING/MONITORING AGENCY NAME(S) AND ADDRESS(ES)

Office of Naval Research
Code 321OA
800 N. Quincy St.
Arlington, VA 22217-5600

10. SPONSOR/MONITOR'S ACRONYM(S)

ONR

11. SPONSOR/MONITOR'S REPORT NUMBER(S)

12. DISTRIBUTION/AVAILABILITY STATEMENT

DISTRIBUTION STATEMENT A
Approved for Public Release
Distribution Unlimited

13. SUPPLEMENTARY NOTES

14. ABSTRACT

A total-field scattered-field (TFSF) boundary can be used to introduce incident plane waves into finite-difference time-domain (FDTD) simulations. For fields which are traveling obliquely to the grid axes, there is no simple way to account fully for the effects of the inherent numerical artifacts associated with plane-wave propagation in the FDTD grid. Failure to account for these artifacts causes erroneous fields to leak across the TFSF boundary. The work performed under this grant developed a TFSF boundary for problems involving a planar interface that is theoretically exact. Such a boundary is essential when modeling the scattering from objects in the vicinity of ocean sediment. Although the TFSF boundary assumes a planar interface, the actual interface used in a simulation can take any shape and the space within the total-field region is arbitrary. A suite of C programs was written to implement the boundary.

15. SUBJECT TERMS

FDTD techniques; propagation and scattering

16. SECURITY CLASSIFICATION OF:			17. LIMITATION OF ABSTRACT	18. NUMBER OF PAGES	19a. NAME OF RESPONSIBLE PERSON
a. REPORT	b. ABSTRACT	c. THIS PAGE	UU	42	John B. Schneider
U	U	U			19b. TELEPHONE NUMBER *(Include area code)* 509 335 4655

INSTRUCTIONS FOR COMPLETING SF 298

1. REPORT DATE. Full publication date, including day, month, if available. Must cite at least the year and be Year 2000 compliant, e.g. 30-06-1998; xx-06-1998; xx-xx-1998.

2. REPORT TYPE. State the type of report, such as final, technical, interim, memorandum, master's thesis, progress, quarterly, research, special, group study, etc.

3. DATES COVERED. Indicate the time during which the work was performed and the report was written, e.g., Jun 1997 - Jun 1998; 1-10 Jun 1996; May - Nov 1998; Nov 1998.

4. TITLE. Enter title and subtitle with volume number and part number, if applicable. On classified documents, enter the title classification in parentheses.

5a. CONTRACT NUMBER. Enter all contract numbers as they appear in the report, e.g. F33615-86-C-5169.

5b. GRANT NUMBER. Enter all grant numbers as they appear in the report, e.g. AFOSR-82-1234.

5c. PROGRAM ELEMENT NUMBER. Enter all program element numbers as they appear in the report, e.g. 61101A.

5d. PROJECT NUMBER. Enter all project numbers as they appear in the report, e.g. 1F665702D1257; ILIR.

5e. TASK NUMBER. Enter all task numbers as they appear in the report, e.g. 05; RF0330201; T4112.

5f. WORK UNIT NUMBER. Enter all work unit numbers as they appear in the report, e.g. 001; AFAPL30480105.

6. AUTHOR(S). Enter name(s) of person(s) responsible for writing the report, performing the research, or credited with the content of the report. The form of entry is the last name, first name, middle initial, and additional qualifiers separated by commas, e.g. Smith, Richard, J, Jr.

7. PERFORMING ORGANIZATION NAME(S) AND ADDRESS(ES). Self-explanatory.

8. PERFORMING ORGANIZATION REPORT NUMBER. Enter all unique alphanumeric report numbers assigned by the performing organization, e.g. BRL-1234; AFWL-TR-85-4017-Vol-21-PT-2.

9. SPONSORING/MONITORING AGENCY NAME(S) AND ADDRESS(ES). Enter the name and address of the organization(s) financially responsible for and monitoring the work.

10. SPONSOR/MONITOR'S ACRONYM(S). Enter, if available, e.g. BRL, ARDEC, NADC.

11. SPONSOR/MONITOR'S REPORT NUMBER(S). Enter report number as assigned by the sponsoring/ monitoring agency, if available, e.g. BRL-TR-829; -215.

12. DISTRIBUTION/AVAILABILITY STATEMENT. Use agency-mandated availability statements to indicate the public availability or distribution limitations of the report. If additional limitations/ restrictions or special markings are indicated, follow agency authorization procedures, e.g. RD/FRD, PROPIN, ITAR, etc. Include copyright information.

13. SUPPLEMENTARY NOTES. Enter information not included elsewhere such as: prepared in cooperation with; translation of; report supersedes; old edition number, etc.

14. ABSTRACT. A brief (approximately 200 words) factual summary of the most significant information.

15. SUBJECT TERMS. Key words or phrases identifying major concepts in the report.

16. SECURITY CLASSIFICATION. Enter security classification in accordance with security classification regulations, e.g. U, C, S, etc. If this form contains classified information, stamp classification level on the top and bottom of this page.

17. LIMITATION OF ABSTRACT. This block must be completed to assign a distribution limitation to the abstract. Enter UU (Unclassified Unlimited) or SAR (Same as Report). An entry in this block is necessary if the abstract is to be limited.

Final Report: Time-Domain Simulations of Problems in Ocean Acoustics

John B. Schneider

School of Electrical Engineering and Computer Science

Washington State University

P.O. Box 642752

Pullman, WA 99164-2752

phone: (509) 335-4655; FAX: (509) 335-3818; email: schneidj@eecs.wsu.edu

http://www.eecs.wsu.edu/~schneidj/

Abstract

A total-field scattered-field (TFSF) boundary can be used to introduce incident plane waves into finite-difference time-domain (FDTD) simulations. For fields which are traveling obliquely to the grid axes, there is no simple way to account fully for the effects of the inherent numerical artifacts associated with plane-wave propagation in the FDTD grid. Failure to account for these artifacts causes erroneous fields to leak across the TFSF boundary. The work performed under this grant developed a TFSF boundary for problems involving a planar interface that is theoretically exact. Such a boundary is essential when modeling the scattering from objects in the vicinity of ocean sediment. Although the TFSF boundary assumes a planar interface, the actual interface used in a simulation can take any shape and the space within the total-field region is arbitrary. A suite of C programs was written to implement the boundary.

1 Introduction

The total-field scattered-field (TFSF) formulation is a method for introducing energy into a finite-difference time-domain (FDTD) simulation. It defines a boundary, identified as the TFSF boundary, which divides the computational domain into two regions: a total-field (TF) region which contains both the incident field and any scattered field, and a scattered-field (SF) region which contains only scattered fields. Scatterers are confined to exist within the TF region. Throughout the grid the fields must have self-consistent update equations meaning that nodes in the TF region must depend on the total field at neighboring nodes while nodes in the SF region must depend on the scattered field at neighboring nodes. However, nodes which are tangential to the TFSF boundary will have at least one neighboring node in the region different from their own. Rectification of this inconsistency is what drives the TFSF method.

Given knowledge of the incident field which should exist at nodes tangential to the TFSF boundary, one does the following. For the update of a node which is in the TF region and depends on a neighboring node in the SF region, the incident field is added to that neighboring node. Conversely, for the update of a node which is in the SF region and depends on a neighboring node in TF region, the incident field is subtracted from that neighboring node. In this way the TFSF boundary acts as a Huygens surface and was originally described as such by Merewether *et al.* [1].

1

In order to implement the TFSF method, one must know the incident field at every time-step at all the tangential nodes adjacent to the boundary. Historically the TFSF method has been used to introduce plane waves into the grid, but in theory any incident field could be realized. In this work we restricted ourselves to plane waves. In the continuous world, the analytic description of pulsed plane-wave propagation is relatively trivial. Unfortunately, because of the inherent difference between the way in which waves propagate in the FDTD grid and the way in which they propagate in the continuous world, one should not simply use the continuous-world expression for the incident plane wave. If one were to do that, the mismatch between the analytic description of the incident field and how the incident field actually propagates within the grid causes fields to leak across the TFSF boundary (in the absence of a scatterer, no fields should be present in the SF region). Fortunately there is a relatively simple fix to this problem.

An auxiliary one-dimensional (1D) FDTD simulation can be implemented to model the propagation of the incident plane wave. If the propagation direction of the incident field in a higher-dimensional grid is aligned with one of the grid axes, the auxiliary 1D grid can be used to describe exactly the incident field at all nodes adjacent to the TFSF boundary. There is no leakage. A detailed discussion of the implementation can be found in [2].

When the incident field propagates obliquely, a one-dimensional auxiliary grid can still be used to describe, at least approximately, the incident field. However, using these fields in the higher-dimensional simulation has inherent errors. First, interpolation must be used to find the fields at points on the 1D grid corresponding to the projected locations of nodes in the higher-dimensional grid. Implementation details for oblique propagation can also be found in [2]. Second, the dispersion which the fields experience in the 1D grid does not correspond to the dispersion experienced in the higher-dimensional grid. To help rectify this, Guiffaut and Mahdjoubi [3] proposed a technique which modified the Courant number in the auxiliary grid so that the dispersion nearly matched that of the higher-dimensional grid (see also Sec. 5.9.1 of [2]). Nevertheless, there are still differences between propagation in the two grids and the need for interpolation, which inherently introduces errors, still exists. Third, the orientation of vector fields (i.e., the velocity field in acoustic simulations and either the electric of magnetic field in electromagnetic simulations) is not the same in the FDTD grid as it is in the continuous world. This fact is discussed in [4,5] and had been considered previously in [6,7]. The orientation is dependent on frequency and hence a simple scalar cannot be used to project field components from a 1D grid to a higher-dimensional grid.

Instead of employing an auxiliary grid, two recent papers proposed a technique where the incident field is obtained analytically by way of the FDTD dispersion relation [4,5]. To distinguish this approach from that which relies upon auxiliary grids, we label this approach the analytic field propagation (AFP) TFSF technique. Moss et al. considered the situation of an electromagnetic field incident on layered uniaxial anisotropic media and hence had to account for the reflection and transmission coefficients of the layers [4]. Schneider restricted consideration to propagation in a homogeneous space [5].

Because of the complexity of the media being considered by Moss et al., the equations given in their work masked the simplicity which pertains for problems involving isotropic media and problems involving a plane satisfying a Dirichlet boundary condition. A Dirichlet boundary in an electromagnetic simulation is equivalent to either a pressure-release or rigid boundary in an

acoustic simulation depending on the polarization assumed. We identify such a boundary a perfect electrically conducting (PEC) boundary. In this report we examined these problems in some detail and obtained equations which are significantly simpler than those presented for anisotropic media. As described both by Moss *et al.* [4] and Schneider [5], the AFP TFSF method requires Fourier transforms to obtain the incident field. However, neither of those papers provided details of the type of transform actually need. In fact, an exact implementation requires not a discrete Fourier transform but rather a discrete-time Fourier transform (which involves a continuous integral). As will be discussed, this transform can be approximated by a discrete transform, but one should be aware of the inherent approximation.

This report begins by discussing the relationship between acoustic and electromagnetic FDTD simulations. The remainder of the work is presented in terms of electromagnetics. An overview of the AFP TFSF technique is then presented that discusses the issues concerning the Fourier transform. We then consider problems involving a PEC plane or a boundary between two half spaces. Both TE and TM polarization are considered. As will be shown, these two-dimensional simulations are analogs of the acoustic problem where the single scalar field (i.e., the magnetic field in the case of TE polarization and electric field in the case of TM polarization) can be equated with pressure and the vector field with velocity. Initially we restrict ourselves to lossless material but then consider lossy material and incidence angles beyond the critical angle. Finally, there is a discussion of the use of the the AFP TFSF technique in three dimensional simulations. Part of the work described here has been accepted for publication in the *IEEE Transactions on Antennas and Propagation*. Another paper, also based on the work presented here, has been submitted to the same journal and is currently in review.

2 Relationship between Acoustic and Electromagnetic FDTD Grids

The FDTD method employs finite-differences to approximate Ampere's and Faraday's laws. Ampere's and Faraday's laws are first-order differential equations which couple the electric and magnetics fields. As we have seen, with a judicious discretization of space and time, the resulting equations can be solved for "future" fields in terms of known past fields.

Other physical phenomena are also described by coupled first-order differential equations where the temporal derivative of one field is related to the spatial derivative of another field. Both acoustics and elastic wave propagation are such phenomena. Here we will consider only acoustic propagation. Specifically we will consider small-signal acoustics which can be described in terms of the scalar pressure field $P(x, y, z, t)$ and the vector velocity $\mathbf{v}(x, y, z, t)$. The material parameters are the speed of sound c_a and the density ρ (both of which can vary as a function of position).

The governing acoustic equations in three dimensions are

$$\frac{\partial P}{\partial t} = -\rho c_a^2 \nabla \cdot \mathbf{v}, \tag{1}$$

$$\frac{\partial \mathbf{v}}{\partial t} = -\frac{1}{\rho} \nabla P, \tag{2}$$

or, expanded in terms of the components,

$$\frac{\partial p}{\partial t} = -\rho c_a^2 \left(\frac{\partial v_x}{\partial x} + \frac{\partial v_y}{\partial y} + \frac{\partial v_z}{\partial z} \right), \tag{3}$$

$$\frac{\partial v_x}{\partial t} = -\frac{1}{\rho} \frac{\partial p}{\partial x}, \tag{4}$$

$$\frac{\partial v_y}{\partial t} = -\frac{1}{\rho} \frac{\partial p}{\partial y}, \tag{5}$$

$$\frac{\partial v_z}{\partial t} = -\frac{1}{\rho} \frac{\partial p}{\partial z}. \tag{6}$$

Equation (2) is essentially a variation of Newton's second law, $F = ma$, where instead of acceleration a there is the derivative of the velocity, instead of mass m there is the mass density, and instead of force F there is the derivative of pressure (which is a force per area and the negative sign accounts for the fact that if pressure is building in a particular direction that tends to cause acceleration in the opposite direction). Equation (1) comes from an equation of state for the material (with various approximations assumed along the way).

Taking the divergence of (2) and interchanging the order of temporal and spatial differentiation yields

$$\frac{\partial}{\partial t} \nabla \cdot \mathbf{v} = -\frac{1}{\rho} \nabla^2 P. \tag{7}$$

Taking the temporal derivative of (1) and using (7) yields

$$\frac{\partial^2 P}{\partial t^2} = -\rho c_a^2 \frac{\partial}{\partial t} \nabla \cdot \mathbf{v} = c_a^2 \nabla^2 P. \tag{8}$$

Rearranging this yields the wave equation

$$\nabla^2 P - \frac{1}{c_a^2} \frac{\partial^2 P}{\partial t^2} = 0. \tag{9}$$

Thus the usual techniques and solutions one is familiar with from electromagnetics carry over to acoustics. For example, a harmonic plane wave given by

$$P(x, y, z, t) = P_0 e^{-j\mathbf{k}\cdot\mathbf{r}} e^{j\omega t} \tag{10}$$

is a valid solution to the governing equations where P_0 is a constant and the wave vector $\mathbf{k}$ can be written

$$\mathbf{k} = k_x \mathbf{a}_x + k_y \mathbf{a}_y + k_z \mathbf{a}_z = k \mathbf{a}_k = (\omega/c_a) \mathbf{a}_k. \tag{11}$$

Substituting (10) into (4) and assuming $\exp(j\omega t)$ temporal dependence yields

$$j\omega v_x = \frac{1}{\rho}(-jk_x)P. \tag{12}$$

Rearranging terms gives

$$v_x = \frac{k_x}{\rho\omega} P. \tag{13}$$

4

Following the same steps for the y and z components produces

$$v_y = \frac{k_y}{\rho\omega}P, \tag{14}$$

$$v_z = \frac{k_z}{\rho\omega}P. \tag{15}$$

Thus the harmonic velocity is given by

$$\mathbf{v} = v_x\mathbf{a}_x + v_y\mathbf{a}_y + v_z\mathbf{a}_z = \frac{1}{\rho\omega}(k_x\mathbf{a}_x + k_y\mathbf{a}_y + k_z\mathbf{a}_z)P = \frac{k}{\rho\omega}P\mathbf{a}_k. \tag{16}$$

Since the wave number, i.e., the magnitude of the wave vector, is given by $k = \omega/c_a$, the ratio of the magnitude of pressure to the velocity is given by

$$\left|\frac{P}{\mathbf{v}}\right| = \rho c_a. \tag{17}$$

The term on the right-hand side is known as the characteristic impedance of the medium which is often written as Z.

2.1 Governing FDTD Equations

To obtain an FDTD algorithm for acoustic propagation, the pressure and components of velocity are discretized in both time and space. In electromagnetics there are two vector fields and hence six field-components which have to be arranged in space-time. In acoustics there is one scalar field and one vector field. Thus there are only four field-components.

To implement a 3D acoustic FDTD algorithm, a suitable arrangement of nodes is as shown in Fig. 1. A pressure node is surrounded by velocity components such that the components are oriented along the line joining the component and the pressure node. This should be contrasted to the arrangement of nodes in electromagnetic grids where the components of the magnetic field swirled around the components of the electric field, and vice versa. In electromagnetics one is modeling coupled curl equations where the partial derivatives are related to behavior orthogonal to the direction of the derivative. In acoustics, where the governing equations involve the divergence and gradient, the partial derivatives are associated with behavior in the direction of the derivative.

The arrangement of nodes in a 2D grid is illustrated in Fig. 2. (This should can be compared to the 2D electromagnetic grids which will be discussed later, i.e., Fig. 6 for the TE^z case and Fig. 8 for the TM^z case.) Because pressure is inherently an acoustic field, there are not two different polarization associated with 2D acoustic simulations—nor is there a notion of polarization in three dimensions.

In addition to the spatial offsets, the pressure nodes are assumed to be offset a half temporal step from the velocity nodes (but all the velocity components exist at the same time-step). The following notation will be used with an implicit understanding of spatial offsets

$$p(x,y,z,t) = P(m\Delta x, n\Delta y, p\Delta z, q\Delta t) = P^q[m,n,p], \tag{18}$$

$$v_x(x,y,z,t) = v_x([m+1/2]\Delta x, n\Delta y, p\Delta z, [q+1/2]\Delta t) = v_x^{q+1/2}[m,n,p], \tag{19}$$

$$v_y(x,y,z,t) = v_y(m\Delta x, [n+1/2]\Delta y, p\Delta z, [q+1/2]\Delta t) = v_y^{q+1/2}[m,n,p], \tag{20}$$

$$v_z(x,y,z,t) = v_z(m\Delta x, n\Delta y, [p+1/2]\Delta z, [q+1/2]\Delta t) = v_z^{q+1/2}[m,n,p]. \tag{21}$$
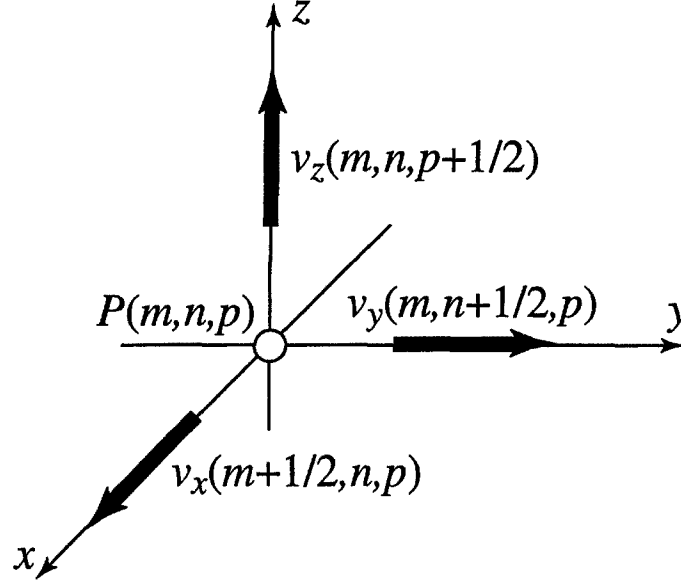
5

Figure 1: An acoustic unit cell in three dimensions showing the arrangement of velocity nodes relative to the pressure node with the same spatial indices.

We will assume the spatial step sizes are the same, i.e., $\Delta x = \Delta y = \Delta z = \delta$.

Replacing the derivatives in (3) with finite differences and using the discretization of (18)–(21) yields the following update equation:

$$
\begin{aligned}
P^q[m,n,p] \;=\; & P^{q-1}[m,n,p] - \rho c_a^2 \frac{\Delta t}{\delta} \left(v_x^{q-1/2}[m,n,p] - v_x^{q-1/2}[m-1,n,p] + \right. \\
& v_y^{q-1/2}[m,n,p] - v_y^{q-1/2}[m,n-1,p] + \\
& \left. v_z^{q-1/2}[m,n,p] - v_z^{q-1/2}[m,n,p-1] \right).
\end{aligned}
\tag{22}
$$

The sound speed and the density can be functions of space. Let us assume that the density and sound speed are specified at the grid points corresponding to the location of pressure nodes. Additionally, assume that the sound speed can be defined in terms of a background sound speed c_0 and a relative sound speed c_r:

$$
c_a = c_r c_0.
\tag{23}
$$

The background sound speed corresponds to the fastest speed of propagation at any location in the grid so that $c_r \leq 1$. The coefficient of the spatial finite-difference in (22) can now be written

$$
\rho c_a^2 \frac{\Delta t}{\delta} = \rho c_r^2 c_0 \frac{c_0 \Delta t}{\delta} = \rho c_r^2 c_0 S_c
\tag{24}
$$

where, similar to electromagnetics, the Courant number is $S_c = c_0 \Delta t / \delta$. The explicit spatial dependence of the density and sound speed can be emphasized by writing the coefficient as
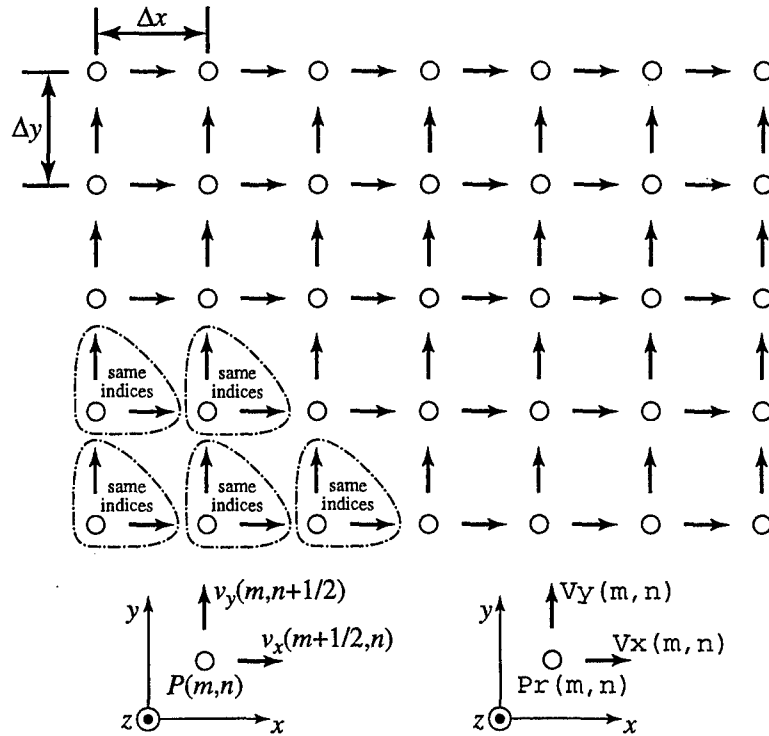
$$
\rho[m,n,p] c_r^2[m,n,p] c_0 S_c
\tag{25}
$$

6

Figure 2: The arrangement of nodes in a 2D acoustic simulation. In a computer FDTD implementation the nodes shown within the dashed enclosures will have the same spatial indices. This is illustrated by the two depictions of a unit cell at the bottom of the figure. The one on the left shows the nodes with the spatial offsets given explicitly. The one on the right shows the corresponding node designations which would be used in a computer program. (Here Pr is used for the pressure array.)

where $\rho[m, n, p]$ is the density which exists at the same point as the pressure node $P[m, n, p]$ and $c_r[m, n, p]$ is the relative sound speed which exists at this same point. Note that the Courant number S_c and the background sound speed c_0 are independent of position. Furthermore, the entire coefficient is independent of time.

The update equation for the x component of velocity is obtained from the discretized version of (4) which yields

$$v_x^{q+1/2}[m, n, p] = v_x^{q-1/2}[m, n, p] - \frac{1}{\rho}\frac{\Delta t}{\delta}\left(P^q[m + 1, n, p] - P^q[m, n, p]\right) \qquad (26)$$

The coefficient of this equation does not contain the Courant number but that can be obtained by multiplying and dividing by the background sound speed

$$\frac{1}{\rho}\frac{\Delta t}{\delta} = \frac{1}{\rho c_0}\frac{c_0 \Delta t}{\delta} = \frac{1}{\rho c_0}S_c. \qquad (27)$$

We wish to define the density only at the pressure nodes. Since the x-component of the velocity is offset from the pressure a half spatial step in the x direction, what is the appropriate velocity to use? The answer, much as it is in the case of an interface between two different materials in electromagnetics, is the average of the densities to either side of the pressure node (where the notion of "either side" is dictated by the orientation of the velocity node). Therefore the coefficient can be written

$$\frac{1}{\left(\frac{\rho[m+1, n, p] + \rho[m, n, p]}{2}\right)c_0}S_c = \frac{2S_c}{(\rho[m + 1, n, p] + \rho[m, n, p])c_0}. \qquad (28)$$

The update equations for the velocity components can now be written as

$$
\begin{aligned}
v_x^{q+1/2}[m, n, p] &= v_x^{q-1/2}[m, n, p] - \\
&\quad \frac{2S_c}{(\rho[m, n, p] + \rho[m + 1, n, p])c_0}\left(P^q[m + 1, n, p] - P^q[m, n, p]\right), \qquad (29) \\
v_y^{q+1/2}[m, n, p] &= v_y^{q-1/2}[m, n, p] - \\
&\quad \frac{2S_c}{(\rho[m, n, p] + \rho[m, n + 1, p])c_0}\left(P^q[m, n + 1, p] - P^q[m, n, p]\right), \qquad (30) \\
v_z^{q+1/2}[m, n, p] &= v_z^{q-1/2}[m, n, p] - \\
&\quad \frac{2S_c}{(\rho[m, n, p] + \rho[m, n, p + 1])c_0}\left(P^q[m, n, p + 1] - P^q[m, n, p]\right). \qquad (31)
\end{aligned}
$$

2.2 Two-Dimensional Implementation

Let us consider a 2D simulation in which the fields vary in the x and y directions. The grid would be as shown in Fig. 2 and it is assumed that $\Delta x = \Delta y = \delta$. Assume the arrays pr, vx, and vy hold the pressure, x component of the velocity, and the y component of the velocity, respectively. Assume the macros Pr, Vx, and Vy have been created to facilitate accessing these arrays. The update equations can be written

8

```
Vx(m,n)  =  Vx(m,n)  -  Cvxp(m,n)*(Pr(m+1,n)  -  Pr(m,n));
Vy(m,n)  =  Vy(m,n)  -  Cvyp(m,n)*(Pr(m,n+1)  -  Pr(m,n));
Pr(m,n)  =  Pr(m,n)  -  Cprv(m,n)*((Vx(m,n)  -  Vx(m-1,n))
                                  +  (Vy(m,n)  -  Vy(m,n-1)));
```

where the coefficient arrays are given by

$$C_{vxp}(m,n) \;=\; \frac{1}{\rho c_0} S_c \bigg|_{(m+1/2)\delta, n\delta} \;=\; \frac{2S_c}{(\rho[m+1,n]+\rho[m,n])c_0}, \tag{32}$$

$$C_{vyp}(m,n) \;=\; \frac{1}{\rho c_0} S_c \bigg|_{m\delta, (n+1/2)\delta} \;=\; \frac{2S_c}{(\rho[m,n]+\rho[m,n+1])c_0}, \tag{33}$$

$$C_{prv}(m,n) \;=\; \rho[m,n]c_r^2[m,n]c_0 S_c. \tag{34}$$

These update equations are little different from those for the TM^z case. The TM^z update equations are

```
Hy(m,n)  =  Hy(m,n)  +  Chye(m,n)*(Ez(m+1,n)  -  Ez(m,n));
Hx(m,n)  =  Hx(m,n)  -  Chxe(m,n)*(Ez(m,n+1)  -  Ez(m,n));
Ez(m,n)  =  Ez(m,n)  +  Cezh(m,n)*((Hy(m,n)  -  Hy(m-1,n))
                                  -(Hx(m,n)  -  Hx(m,n-1)));
```

There is a one-to-one mapping between these sets of equations. One can equate values as follows

$$v_x \;\Leftrightarrow\; -H_y, \tag{35}$$

$$v_y \;\Leftrightarrow\; H_x, \tag{36}$$

$$P \;\Leftrightarrow\; E_z, \tag{37}$$

$$C_{vxp} \;\Leftrightarrow\; C_{hye}, \tag{38}$$

$$C_{vyp} \;\Leftrightarrow\; C_{hxe}, \tag{39}$$

$$C_{prv} \;\Leftrightarrow\; C_{ezh}. \tag{40}$$

Thus, converting 2D programs which were written to model electromagnetic field propagation to ones which can model acoustic propagation is surprisingly straightforward. Essentially, all one has to do is change some labels and a few signs.

For TE^z simulations, the updated equations for a lossless medium are

```
Hz(m,n)  =  Hz(m,n)  +
            Chze(m,n)*((Ex(m,n+1)-Ex(m,n))-(Ey(m+1,n)-Ey(m,n)));
Ex(m,n)  =  Ex(m,n)  +  Cexh(m,n)*(Hz(m,n)-Hz(m,n-1));
Ey(m,n)  =  Ey(m,n)  -  Ceyh(m,n)*(Hz(m,n)-Hz(m-1,n));
```

In this case the conversion from the electromagnetic equations to the acoustic equations can be accomplished with the following mapping

$$v_x \quad \Leftrightarrow \quad E_y, \tag{41}$$

$$v_y \quad \Leftrightarrow \quad -E_x, \tag{42}$$

$$P \quad \Leftrightarrow \quad H_z, \tag{43}$$

$$C_{vxp} \quad \Leftrightarrow \quad C_{eyh}, \tag{44}$$

$$C_{vyp} \quad \Leftrightarrow \quad C_{exh}, \tag{45}$$

$$C_{prv} \quad \Leftrightarrow \quad C_{hxe}. \tag{46}$$

For three dimensions 3D acoustic code is arguably simpler than the electromagnetic case since there are not two vector fields. However porting 3D electromagnetic algorithms to the acoustic case is not as trivial as in two dimensions.

3   The AFP TFSF Method

Any implementation of a TFSF boundary requires knowledge of the incident field at nodes adjacent to the boundary for every time-step of the simulation. Conceptually, the AFP version of the TFSF method is quite simple in that it parallels the usual description of propagation in the continuous world.

In the continuous world, the spatial dependence of a harmonic plane wave is given by $\exp(-j\mathbf{k}\cdot\mathbf{r})$ where $\mathbf{k}$ is the wave vector and $\mathbf{r}$ is the position vector ($\exp(j\omega t)$ temporal dependence is understood). For a pulsed plane wave each spectral component can be weighted by the appropriate amount to give the frequency-domain representation. So, for example, if a field component were found at the origin to be given in the time-domain by $f(t)$, its frequency-domain representation would be $F(\omega) = \mathcal{F}[f(t)]$ where $\mathcal{F}[]$ is the Fourier transform. The field at an arbitrary point $\mathbf{r}$ merely has to account for the displacement from the origin. Thus in the frequency domain the field is given by $F(\mathbf{r}, \omega) = F(\omega)\exp(-j\mathbf{k}\cdot\mathbf{r})$. The time-domain signal at $\mathbf{r}$ is the inverse transform of this, i.e.,

$$f(\mathbf{r}, t) = \frac{1}{2\pi} \int_{-\infty}^{\infty} F(\omega) e^{-j\mathbf{k}\cdot\mathbf{r}} e^{j\omega t} d\omega. \tag{47}$$

Assuming lossless media, in the continuous world the magnitude of the wave vector is given by ω/c where c is the speed of light. Thus it is straightforward to evaluate (47)—the complex exponential involving space merely represents a shift operation.

In the discretized world of the FDTD method, one can follow steps which parallel those in the continuous world. However, finding the field at an arbitrary point is complicated by the fact that the wave vector in the grid is governed by the FDTD dispersion relation which does not, in general, have a closed-form solution. Nevertheless, it is relatively easy to solve for the wave vector and to perform the necessary transforms to calculate the incident field wherever it is needed.

Since the input signal is not periodic, one cannot use a discrete Fourier transform (which inherently assumes a periodic signal). Instead, for a transient signal, one must use the discrete-time

Fourier transform [8]. The inverse and forward transforms of the discrete signal $f(q\Delta_t) = f[q]$ are given by

$$f[q] = \frac{1}{2\pi} \int_0^{2\pi} F(\omega')e^{j\omega' q}d\omega', \tag{48}$$

$$F(\omega') = \sum_{q=-\infty}^{\infty} f[q]e^{-j\omega' q}. \tag{49}$$

Note that, despite this transform pertaining to a discretized world, the frequency ω' is a continuous variable. In FDTD, any "source function" $f[q]$ can be assumed to start at $q = 0$ and be limited to a maximum of N_s time steps (i.e., the source function has either decayed to zero at time-step N_s or is switched off at time-step N_s—this could correspond to the time at which the simulation is terminated). Thus (49) can be written

$$F(\omega') = \sum_{q=0}^{N_s-1} f[q]e^{-j\omega' q}. \tag{50}$$

For the sake of illustration, consider a 1D computational domain in which the source-function $f[q]$ represents the time-varying field at some point. Further assume this field is propagating in the positive x direction. The field at a point which is m spatial steps away from where $f[q]$ is measured would be given by

$$f[m, q] = \frac{1}{2\pi} \int_0^{2\pi} F(\omega')e^{-j\tilde{k}\delta m}e^{j\omega' q}d\omega' \tag{51}$$

where $\tilde{k}$ is the numeric wavenumber and δ is the spatial step size. Equation (51) is the 1D FDTD analog of (47). In one dimension a closed-form expression can be obtained for $\tilde{k}\delta$:

$$\tilde{k}\delta = 2\sin^{-1}\left(\frac{1}{S_c}\sin\left(\frac{\omega'}{2}\right)\right) \tag{52}$$

where S_c is the Courant number. (One can equate ω' with the more familiar $\omega\Delta_t$ which typically appears in the FDTD dispersion relation, but the fact remains that ω' varies continuously in the integral of (51).)

Knowing the direction of propagation and the incident field at a given point (i.e., $f[q]$), one can calculate $F(\omega')$ using (50) and then find the field at an arbitrary point $f[m, q]$ using (51). This was done in [9] where it was shown how this approach could predict the superluminal component of FDTD propagation. It was speculated in [9] that this technique could be used to realize a TFSF boundary which would essentially be perfect. Indeed, this approach is at the core of the work by [4] and [5], but neither paper provided details concerning the Fourier transforms nor were details discussed in [9]. (It should also be pointed out that Ma *et al.* [10] have obtained an analytic expression for the field at an arbitrary point in the FDTD grid due to a source which is impulsive both in time and space. That differs from the solution here in that plane waves are of interest. These plane waves may be impulsive in time but cannot, by definition, be impulsive in more than one direction.)

Substituting (49) (after a change of index from q to q') into (51) and rearranging yields

$$f[m,q] = \sum_{q'=0}^{N_s-1} f[q']\frac{1}{2\pi} \int_0^{2\pi} e^{-j\tilde{k}\delta m}e^{j\omega'(q-q')}d\omega'. \tag{53}$$

This equation is exact and the integral possesses some interesting properties (for example, it is zero when $m > (q - q')$). Note that the source function $f[q']$ is assumed to be zero for $q' \geq N_s$ but $f[m,q]$ can be evaluated for any value of q, i.e., it is not bound by N_s. Unfortunately this equation cannot be easily evaluated efficiently nor can it be evaluated without resorting to numerical approximations.

An efficient calculation of this expression is obtained by employing standard discrete Fourier techniques (as was done in [4, 5, 9]). This is equivalent to approximating the integral in (51) as a Riemann sum. Let us assume that N_t equally spaced samples of the integrand are used to approximate the integral. In this case the frequency ω' is given by $2\pi n/N_t$ (where $0 \leq n \leq N_t-1$) and $d\omega'$ is approximately $2\pi/N_t$. An approximation of (51) is thus

$$f[m,q] \approx \frac{1}{2\pi} \sum_{n=0}^{N_t-1} F\left(\frac{2\pi n}{N_t}\right) e^{-j\tilde{k}\delta m}e^{j\frac{2\pi n}{N_t}q}\frac{2\pi}{N_t}. \tag{54}$$

Regrouping terms and employing (50) yields

$$f[m,q] \approx \sum_{n=0}^{N_t-1} \left\{ \frac{1}{N_t} \sum_{q'=0}^{N_s-1} f[q']e^{-j\frac{2\pi n}{N_t}q'} \right\} e^{-j\tilde{k}\delta m}e^{j\frac{2\pi nq}{N_t}}. \tag{55}$$

If one sets N_s equal to N_t (which can be accomplished by zero-padding the source function $f[q']$ to the necessary length), then the term within braces is recognized as the discrete Fourier transform of the source function. This transform is multiplied by $\exp(-j\tilde{k}\delta m)$ and then the inverse discrete Fourier transform is taken. Since discrete Fourier transforms can be calculated efficiently, (55) can be calculated efficiently.

In the implementation of a TFSF boundary, one must calculate fields which are offset both spatially and temporally. Even though two fields are temporally offset by half a time step they still use identical samples of the source function $f[q']$. The offset is accounted for in the inverse transform, i.e.,

$$\begin{aligned} f\left[m+\frac{1}{2}, q+\frac{1}{2}\right] &= \sum_{n=0}^{N_t-1} F(\omega_n)e^{-j\tilde{k}\delta(m+\frac{1}{2})}e^{j\frac{2\pi n(q+1/2)}{N_t}} \\ &= \sum_{n=0}^{N_t-1} F(\omega_n)e^{-j\tilde{k}\delta/2}e^{j\frac{\pi n}{N_t}}e^{-j\tilde{k}\delta m}e^{j\frac{2\pi nq}{N_t}} \end{aligned} \tag{56}$$

where $F(\omega_n)$ is the term in braces in (55). (When calculating the various field components one must also account for the characteristic impedance and the orientation of the fields. This is discussed more later.)

One question which remains is the value which should be chosen for N_t to obtain a good approximation of the exact integral. Naturally, the more points the better the approximation will

12

be, but one can obtain rough guidelines as follows. Using discrete transforms is equivalent to assuming the source function is periodic. However, one does *not* want this periodic behavior to be evident in the simulation. Hence the discrete Fourier transforms must be long enough (i.e., N_t must be great enough) so that virtually all the energy associated with the incident field has traversed the total-field region before the incident field can repeat itself.

For example, consider an incident pulse which is non-zero for 100 time-steps ($N_s = 100$) and which is incident upon a TF region which is 50 spatial steps wide. The inverse transform associated with the last point in the TF region must be sufficiently long so that it can model the time it takes for the incident pulse to propagate to that point and the time it takes for the pulse to completely pass this point. Although the pulse started by being bound by 100 time steps, because of the dispersion in the FDTD grid, it will take more than 100 time steps for the pulse to pass any point. The more distance the pulse has to travel, the more it will disperse. In fact, as discussed in [5, 11, 12], the group velocity in the FDTD grid goes to zero at the coarsest discretizations and hence it arguably takes an infinite time for a pulse to pass completely any point. Nevertheless, in practical applications the coarsest discretization are not of interest. By using a reasonable Courant number and a reasonable discretization of the incident pulse, there will be little spectral content at the coarsest discretization. Thus, in this example, a discrete Fourier transforms of 1024 points (i.e., $N_t = 1024$) would almost certainly be sufficient to describe the incident pulse over the entire TFSF boundary.

The FDTD simulation itself can proceed for any number of time steps. If a highly resonant structure were being illuminated and the user wanted to run the simulation for a hundred-thousand time steps, or more, that would be irrelevant to the implementation of the TFSF boundary. The incident field on the boundary would merely be assumed to be zero after 1024 time steps.

Generalizing (51) to higher dimensions is trivial in that it is nearly identical to (47)—the only differences are the limits of the integral and the use of the discrete wavenumber components. For example, assuming a uniform grid in which $\Delta_x = \Delta_y = \delta$, let the field $f[m, n, q]$ represent the fields at the point $\mathbf{r} = (m\delta, n\delta)$ and time $q\Delta_t$. Given the field $f[q]$ at the origin which has Fourier transform $F(\omega')$, $f[m, n, q]$ is given by

$$f[m, n, q] = \frac{1}{2\pi} \int_0^{2\pi} F(\omega')e^{-j\tilde{\mathbf{k}}\cdot\mathbf{r}}e^{j\omega' q}d\omega'. \tag{57}$$

In this case the components of the numeric wave vector $\tilde{\mathbf{k}}$ must be calculated from the the 2D dispersion relation but the integral can again be approximated with discrete transforms as done in (55). We note that the superluminal wave vector components discussed in [9, 13] are not incorporated in the results to be shown later. These components, which occur at the coarsest discretizations supported by the grid, experience exponential decay as they propagate. Discarding them from the solution slightly increases the amount of leaked fields but this is not a concern in practice (owing to the associated frequencies not being ones which would be of interest and the inherent exponential decay).

Equation (51) gives the spatial and temporal dependence of a single field component. Given a single field component, the polarization, and the direction of propagation, all the other field components can be computed. Despite the characteristic impedance of the FDTD grid being exact,

such a computation is more involved than in the continuous world because of the non-orthogonality of the electric field, magnetic field, and wave vector. Details of the relationship between these three quantities are discussed in [5].

When a halfspace discontinuity is present, one must account for the reflected or, where applicable, the transmitted fields. To demonstrate this, we first consider the case of illumination of a Dirichlet planar boundary, i.e., a PEC plane where there is no transmitted field and the reflection coefficient is -1. We then consider penetrable media which must incorporate the transmission and reflection coefficients.

4 TE^z Polarization and a PEC Plane

Consider a 2D FDTD grid with TE^z polarization in which a PEC plane is assumed, at least insofar as the incident field is concerned, to span the computational domain. This scenario is depicted in Fig. 3. The acoustic pressure can be equated with the magnetic field and the velocity with the electrics field (with an appropriate change of signs). The PEC plane is thus equivalent to a rigid boundary at which the normal component of velocity goes to zero. We define the "incident field" as being the sum of the incoming field (i.e., the field whose x-component of the wave vector is positive) and the reflected field. By doing this, in the absence of any additional scatterers other than the PEC plane itself, the SF region would contain no fields. It is important to note that in any given simulation there are no restrictions on the contents of the TF region. In fact, the PEC plane does not even have to span the TF region. Thus, for example, one can consider the fields associated with obliquely illuminated apertures. In the SF region, however, it is required that the plane is intact and that no other scatterers are present.

Nodes which are tangential to the TFSF boundary and have a neighboring node on the other side of the boundary must have their update-equations corrected to account for the existence of the TFSF boundary (see [2] for details). For the situation considered here, the TFSF boundary is only three-sided. The field is not specified on, or beyond, the PEC. Instead, as is usual when modeling PEC's, the tangential electric fields along the PEC are set to zero and the FDTD algorithm handles the rest.

To implement the TFSF method, the incident field contains two plane waves: the "incoming field" and the reflected field. This scenario is shown in Fig. 4. The "reference point" in Fig. 4 is essentially the origin at which the user would specify the source function $f[q]$. Note that this point does not need to be within the computational domain! Its location is on the PEC and such that for the given incident angle ϕ_i at the start of the simulation the incoming field has not yet entered the TF region (but the leading edge of the field sits poised to enter the region). The field at points along the TFSF boundary are then determined relative to displacement from this reference point in accordance with (57).

One can easily show that the FDTD reflection coefficient for a PEC plane is identically -1 (relative to the electric field) and the details will not be presented here. Suffice it to say that the incoming and reflected fields have the same y components of their wave numbers and equal magnitude but opposite signs for the x components. The Fourier transform of the source function $f[q]$ is taken to be the spectral representation of the magnetic field for both the incoming and
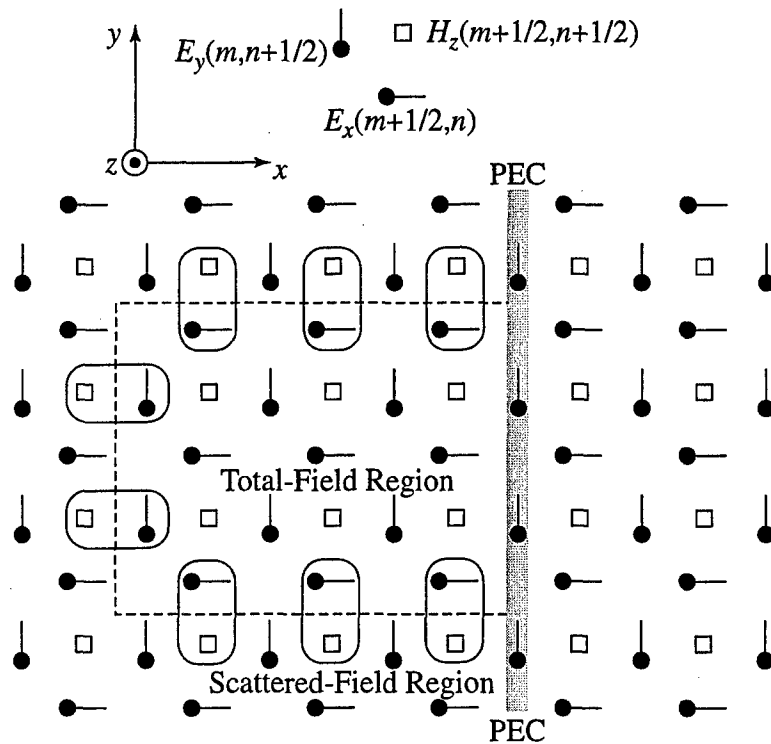
14

Figure 3: Depiction of a TE^z grid containing a PEC plane. The TFSF boundary is drawn with a dashed lines. The nodes enclosed in rounded rectangles must have their values corrected owing to a neighboring node being on the other side of the boundary. In the acoustic analog of this polarization the magnetic field can be equated with the pressure and the electric field with the velocity. The PEC plane is thus equivalent to a rigid boundary.

15

reflected fields. The x and y components of the electric field are found in accordance with the orthogonality condition discussed in [5]. (The incoming and reflected fields have the same sign for the x component of the electric field but opposite signs for the y component.) Thus the incident field is realized by summing two plane waves, each with a common reference point and the same amplitude. The only difference is the direction of propagation. The calculation of each individual plane wave follows the details provided in [5]. The superposition of these waves satisfies the boundary condition dictated by the existence of a PEC plane in the FDTD grid and hence can be used to realize a nearly perfect TFSF boundary.

To illustrate the behavior of this TFSF implementation, consider a pulsed plane wave propagating at an incident angle of 60 degrees. The field is traveling in free space and the Courant number is 95 percent of the 3D limit, i.e., $S_c = 0.95/\sqrt{3}$. This Courant number was chosen so that the results pertain to 3D simulations in which the incident field propagates orthogonal to one of the axes (the factor of 95 percent was chosen somewhat arbitrarily—stability is no more of a concern with this TFSF technique than it is with the surrounding grid). The pulse is a Ricker wavelet discretized so that there are 10 cells per wavelength at the most energetic frequency. With this discretization there is a substantial amount of energy at coarser discretizations (see [5] for further discussion of this source function). One would anticipate this pulse would suffer substantial dispersion as it propagates, something which is undesirable in practice but good for testing the performance of a TFSF implementation. Fig. 5 shows a computational domain which is 180 by 200 cells. A vertical PEC exists 105 cells from the left. The SF region is 15 cells thick. Figure 5(a) shows the magnetic field 150 time-steps into the simulation. The images show the log base 10 of the absolute value of the field and have been scaled so that it is visible over three orders of magnitude. In Fig. 5(a) the incoming field has already encountered the PEC. The TFSF boundary is aware of the reflected field and there is virtually no leakage through the boundary. Fig. 5(b) shows the magnetic field at 350 time steps. The dispersion of the incoming field is clearly evident as the width of the pulse is greater than it had been at 150 time-steps. This dispersion is subsequently evident in the field reflected by the PEC plane. The AFP TFSF implementation automatically incorporates these numeric artifacts. Using a discrete Fourier transform of 1024 points, the peak magnetic field leaked across the boundary in this case is approximately five orders of magnitude down from the peak value of the magnetic field (i.e., 100 dB down from the peak). If one were to use a more reasonable discretization of 20 cells per wavelength at the peak frequency of the pulse, the leaked field drops to 180 dB down from the peak of the incident field. (Note that in Figs. 5(a) and (b) there is no reason to extend the computational domain beyond the PEC boundary since no fields propagate past the PEC. It was done here merely for the sake of consistency with (c) and (d).)

Figure 5(c) also shows the magnetic field over the computational domain at time-step 350, but in this case there are two slits in the PEC plane. Each slit is 10 cells wide and their centers are separated by 40 cells. The field scattered back to the left of the PEC as well as the field which passes through the slits are clearly evident. The implementation of the TFSF boundary is oblivious to the actual contents of the TF region (or to anything beyond the PEC plane).

The diffraction from infinite wedges was studied using the FDTD method in [14, 15]. In that work the TFSF boundary passed through the perfectly matched layer (PML) which terminated the grid. For a field originating in the PML, an amplification factor had to be found to compensate
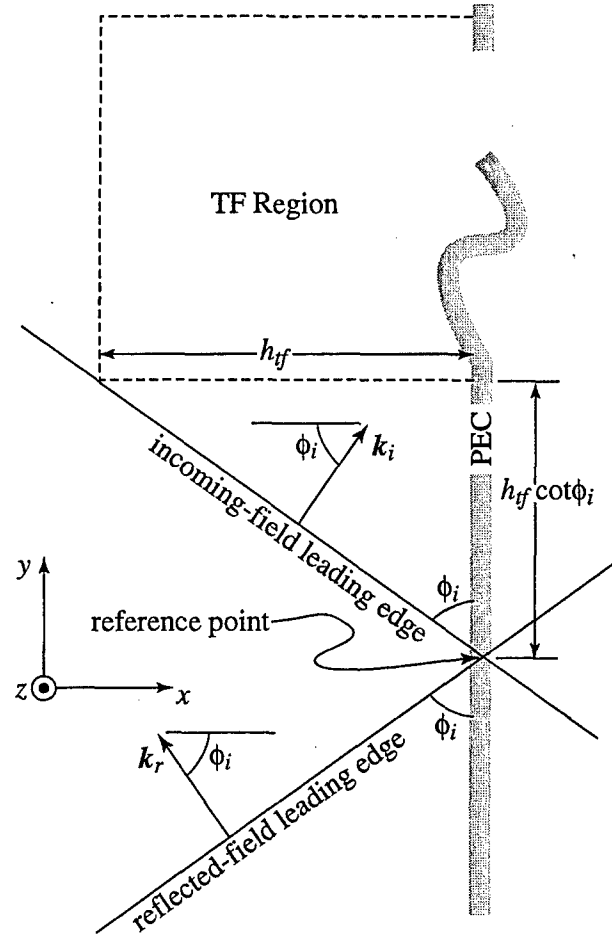
16

Figure 4: To model a PEC boundary, the "incident field" contains both an incoming and a reflected field. The width of the TF region is h_{tf}. The origin, or reference point, for the sake of calculating the incident field is a distance $h_{tf}\cot(\phi_i)$ from the bottom of the TF region. This ensures that the incoming field, which is specified by the source function $f[q]$, is completely outside of the TF region at the start of the simulation. The bending of, and gap in, the PEC boundary is used to emphasize that there are no restrictions on the contents of the TF region. Inhomogeneities can be present throughout the TF region.
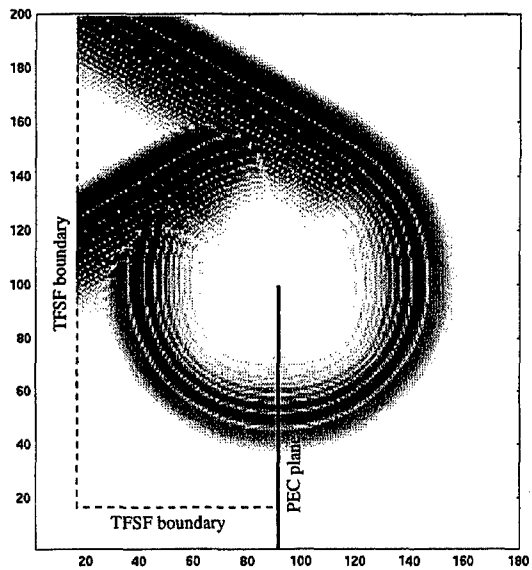
17
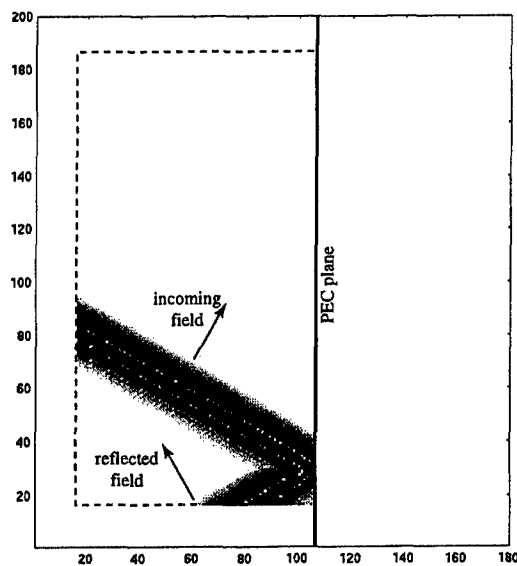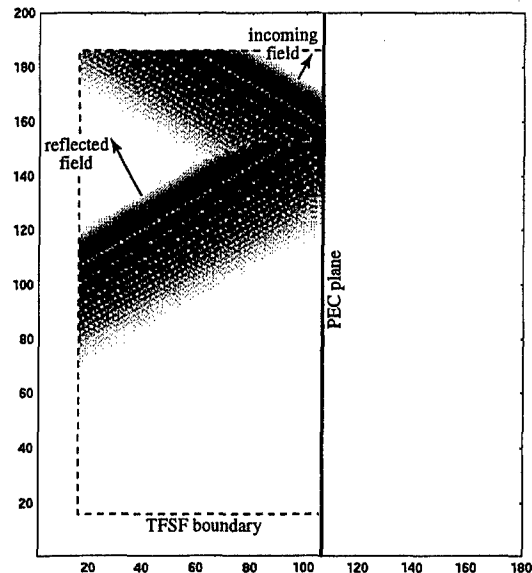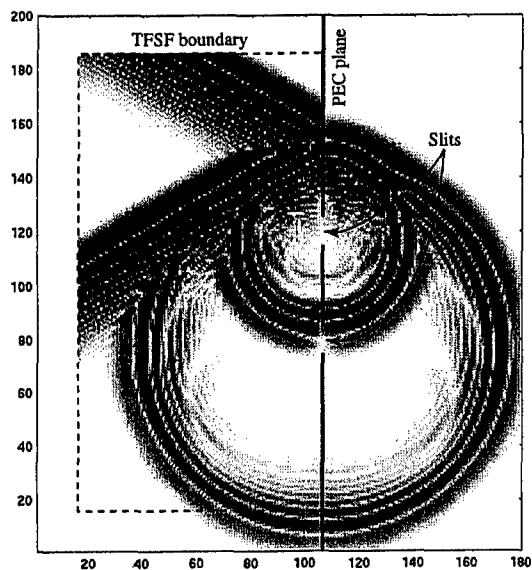
Figure 5: Snapshots of the magnetic field at time-steps (a) 150 and (b) 350. (c) Magnetic field at time-step 350 when two slits are present in the PEC plane. (d) Magnetic field at time-step 350 showing diffraction from the edge of a semi-infinite plane. The incident angle is 60 degrees with respect to horizontal.

18

for the PML loss. Using the AFP TFSF technique, it would not be necessary to have an incoming field start within the PML owing to the fact that the AFP TFSF technique already includes the reflected field. This is illustrated in Fig. 5(d) which shows the diffraction from a "knife edge." This snapshot is also of the magnetic field and at time-step 350. In this case the TFSF boundary is two-sided. One-side, which is drawn vertically, is terminated one cell before the top edge of the computational domain where a second-order Higdon ABC is used. The grid termination would benefit from the use of a PML as described in [14, 15], but no amplification factors would be needed and the reflected field would be completely present at the start of the TFSF boundary. Thus the reflected field would not have to build up from the start of the PEC plane which is within the PML nor would it suffer the corresponding diffraction at that leading edge—there is no "leading edge" of the PEC in the AFP TFSF implementation for the incoming field to encounter. Instead of the knife-edge shown here, wedges could be studied just as easily (and, as will be more clear after considering dielectric boundaries, the technique can be applied to penetrable wedges too).

The AFP TFSF technique allows the calculation of the incoming and/or the reflected field at an arbitrary point. The technique does not care if the point is actually on the TFSF boundary or even if it is within the grid. Thus, when it comes to recording, for example, the diffracted field, the observation points can be placed anywhere in the computational domain. One can subtract the incident or reflected field from the recorded field. In this way, one does not have to restrict observation points to the scattered-field region.

There are other problems which could benefit from the application of the AFP TFSF boundary described here. For example, it provides an alternative way to study the scattering from randomly rough surfaces than the one presented in [16]. In [16] the incident field employed a Gaussian-tapered plane wave as described in [17]. The Gaussian taper was necessary to minimize diffraction errors which would be present if an obliquely incident plane wave were to encounter a finite surface—only a finite amount of the rough surface can be included in any particular simulation. A Gaussian-tapered plane wave is not a true solution to the wave equation. Additionally, the taper is such that a very large computational domain must be used to ensure the fields are small at either end of the tapered wave. On the other hand, using the TFSF implementation described here, the surface is effectively infinite (although the surface roughness must be contained within the TF region). The surface roughness would have to be "turned on" (i.e., ramped up and down so that it met the edges of the planar surface at the TFSF boundary), but this can be done in much less space than the Gaussian tapering of the incident plane wave. Unlike with a Gaussian-tapered incident field, in the AFP TFSF method the incident field is a solution to the wave equation. Thus the AFP TFSF boundary has the potential to provide much more efficient and more accurate solutions to these types of problems.

5 TE^z Polarization with a Dielectric Halfspace

For a field incident on a penetrable halfspace, one must account for both the reflected and transmitted fields and hence must know the reflection and transmission coefficients. Consider a plane wave propagating obliquely in the 2D TE^z grid shown in Fig. 6. The non-zero fields are E_x, E_y, and H_z (this corresponds to the polarization identified as TM in [4]). Again, the acoustic pressure
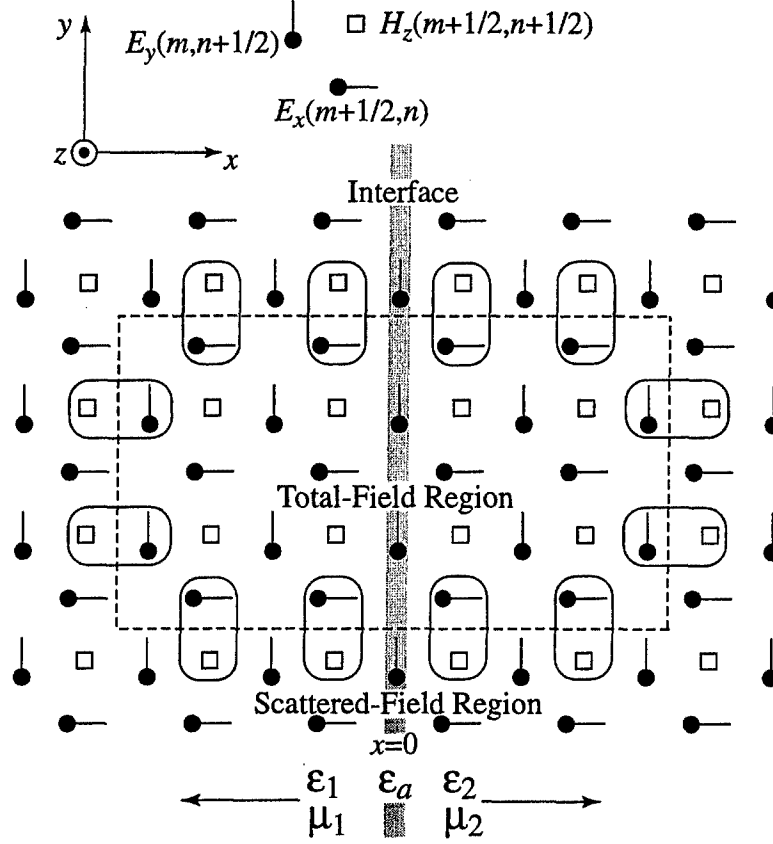
Figure 6: Portion of the TE^z grid. An interface exists at $x = 0$. To the left of the interface the permittivity and permeability are ϵ_1 and μ_1, respectively, and to the right they are ϵ_2 and μ_2. Along the interface the permittivity is ϵ_a. Magnetic fields are unambiguously in the first or second medium and hence always use either μ_1 or μ_2. The acoustic analog of this simulation equates the pressure with the electric field and the velocity with the magnetic field.

can be equated with the magnetic field and the velocity can be equated with the magnetic field. For the sake of simplicity, assume a uniform grid where $\Delta_x = \Delta_y = \delta$. The computational domain consists of two half-spaces where the permittivity and permeability are ϵ_1 and μ_1, respectively, to the left of the interface at $x = 0$ and ϵ_2 and μ_2 to the right. Throughout the following a subscript 1 will be used to indicate quantities to the left of the interface and a subscript 2 will indicate quantities to the right. The E_y nodes along the interface have a permittivity of ϵ_a, the value of which is left arbitrary for now.

We adopt the discrete calculus notation described in [5] (which differs slightly from that use in [4]) and start with the description of an arbitrary harmonic wave. The magnetic field is given by

$$
\begin{aligned}
\hat{\mathbf{H}} &= \mathbf{a}_z \hat{H}_z = \mathbf{a}_z \hat{H}_0 e^{-j(\tilde{k}_x m\delta + \tilde{k}_y n\delta)} e^{j\omega q\Delta_t} \\
&= \mathbf{a}_z \hat{H}_0 e^{-j\tilde{\mathbf{k}}\cdot\mathbf{r}} e^{j\omega q\Delta_t},
\end{aligned}
\tag{58}
$$

where, for propagation at an angle ϕ relative to the x axis, the numeric wave vector $\tilde{\mathbf{k}}$ is

$$
\tilde{\mathbf{k}} = \left(\tilde{k}_x, \tilde{k}_y \right) = \tilde{k} \left(\cos\phi, \sin\phi \right),
\tag{59}
$$

20

ω is the frequency, q is the temporal index, and m and n are the spatial indices in the x and y directions, respectively. The spatial dependence is given by $\exp(-j\tilde{\mathbf{k}} \cdot \mathbf{r})$ where $\mathbf{r} = (m\delta, n\delta)$ (m and n are not restricted to integer values and can be offset by appropriate fractional amounts to account for the staggering of the grid). The corresponding electric field is given by

$$
\begin{aligned}
\hat{\mathbf{E}} &= \mathbf{a}_x \hat{E}_x + \mathbf{a}_y \hat{E}_y = (\mathbf{a}_x \hat{E}_{0x} + \mathbf{a}_y \hat{E}_{0y}) e^{-j\tilde{\mathbf{k}} \cdot \mathbf{r}} e^{j\omega q \Delta_t}, \\
&= \hat{\mathbf{E}}_0 e^{-j\tilde{\mathbf{k}} \cdot \mathbf{r}} e^{j\omega q \Delta_t}.
\end{aligned}
\tag{60}
$$

The vector $\hat{\mathbf{E}}_0$ and scalar $\hat{H}_0$ are constants for a given frequency (but are themselves functions of frequency). A tilde indicates a numeric quantity while a caret implies a quantity is in the frequency domain and may be complex.

Let the shift operator s_ξ^+ shift the ξ-index by $+1/2$ where $\xi \in \{x, y, t\}$. For example,

$$
s_x^+ \hat{\mathbf{E}} = \hat{\mathbf{E}}_0 e^{-j(\tilde{k}_x(m+1/2)\delta + \tilde{k}_y n\delta)} e^{j\omega q \Delta_t} = e^{-j\tilde{k}_x \delta/2} \hat{\mathbf{E}}.
\tag{61}
$$

Conversely, s_ξ^- shifts the ξ-index by $-1/2$. The discrete difference operator $\tilde{\partial}_\xi$ is defined as

$$
\tilde{\partial}_\xi = \frac{1}{\Delta_\xi} \left(s_\xi^+ - s_\xi^- \right).
\tag{62}
$$

For plane-wave propagation, the discrete difference operators can be represented by multiplicative functions. When ξ is either x or y one obtains

$$
\tilde{\partial}_\xi \hat{\mathbf{E}} = -j\frac{2}{\delta} \sin\left(\frac{\tilde{k}_\xi \delta}{2} \right) \hat{\mathbf{E}} = -j K_\xi \hat{\mathbf{E}}.
\tag{63}
$$

Similarly, the temporal finite difference yields

$$
\tilde{\partial}_t \hat{\mathbf{E}} = j\frac{2}{\Delta_t} \sin\left(\frac{\omega \Delta_t}{2} \right) \hat{\mathbf{E}} = j\Omega \hat{\mathbf{E}}.
\tag{64}
$$

The difference operators acting on the magnetic field yield similar results. In terms of these operators the dispersion relationship is given by

$$
\Omega^2 \mu \epsilon = K_x^2 + K_y^2.
\tag{65}
$$

Ignoring the shift operators which are common to both sides, for the two-dimensional propagation which pertains here, the FDTD harmonic form of Ampere's law can be written

$$
j\Omega \epsilon \hat{\mathbf{E}} = -j\mathbf{K} \times \hat{\mathbf{H}} = -j\mathbf{a}_x K_y \hat{H}_z + j\mathbf{a}_y K_x \hat{H}_z,
\tag{66}
$$

where $\mathbf{K} = (K_x, K_y)$ (see [5] for further details including the shift operators which have been dropped). Thus, the components of the electric field are related to the magnetic field via

$$
\hat{E}_x = -\frac{K_y}{\Omega \epsilon} \hat{H}_z,
\tag{67}
$$

$$
\hat{E}_y = \frac{K_x}{\Omega \epsilon} \hat{H}_z.
\tag{68}
$$

21

As mentioned previously, knowing one field component, the polarization, and the direction of propagation, one can obtain all the field components. Equations (67) and (68) demonstrate this is true.

To solve for the reflection and transmission coefficients, one must obtain two independent equations relating them. As in the continuous world, the phase of the incoming, reflected, and transmitted fields must match along the interface. This dictates that the angle of reflection must equal the angle of incidence. Assuming a unit amplitude incoming wave, the incoming, reflected, and transmitted magnetic fields can be written, respectively,

$$\hat{\mathbf{H}}^i = \mathbf{a}_z e^{-j\tilde{\mathbf{k}}_i \cdot \mathbf{r}}, \tag{69}$$

$$\hat{\mathbf{H}}^r = -\mathbf{a}_z \hat{\tilde{\Gamma}}_{te} e^{-j\tilde{\mathbf{k}}_r \cdot \mathbf{r}}, \tag{70}$$

$$\hat{\mathbf{H}}^t = \mathbf{a}_z \hat{\tilde{T}}_{te} e^{-j\tilde{\mathbf{k}}_t \cdot \mathbf{r}}, \tag{71}$$

where

$$\tilde{\mathbf{k}}_i = \mathbf{a}_x \tilde{k}_1 \cos\phi_i + \mathbf{a}_y \tilde{k}_1 \sin\phi_i = (\tilde{k}_{1x}, \tilde{k}_y) \tag{72}$$

$$\tilde{\mathbf{k}}_r = -\mathbf{a}_x \tilde{k}_1 \cos\phi_i + \mathbf{a}_y \tilde{k}_1 \sin\phi_i = (-\tilde{k}_{1x}, \tilde{k}_y), \tag{73}$$

$$\tilde{\mathbf{k}}_t = \mathbf{a}_x \tilde{k}_2 \cos\phi_t + \mathbf{a}_y \tilde{k}_2 \sin\phi_t = (\tilde{k}_{2x}, \tilde{k}_y), \tag{74}$$

$\tilde{k}_1$ and $\tilde{k}_2$ are the FDTD wave numbers in the first and second media, respectively, ϕ_i is the incident angle, ϕ_t is the transmitted angle, and $\hat{\tilde{\Gamma}}_{te}$ and $\hat{\tilde{T}}_{te}$ are the reflection and transmission coefficients, respectively. The temporal dependence which is common to all terms has been dropped. Because of the phase matching which must exist at the interface, $\tilde{k}_1 \sin\phi_i$ must equal $\tilde{k}_2 \sin\phi_t$, i.e., the y component of the wave vector is the same throughout the grid.

The total field in the first medium is the sum of the incoming and reflected waves, i.e.,

$$\hat{\mathbf{H}}_1 = \mathbf{a}_z \left(e^{-j\tilde{\mathbf{k}}_i \cdot \mathbf{r}} - \hat{\tilde{\Gamma}}_{te} e^{-j\tilde{\mathbf{k}}_r \cdot \mathbf{r}} \right), \tag{75}$$

$$\hat{\mathbf{E}}_1 = -\frac{\mathbf{K}^i}{\Omega \epsilon_1} \times \mathbf{a}_z e^{-j\tilde{\mathbf{k}}_i \cdot \mathbf{r}} + \frac{\mathbf{K}^r}{\Omega \epsilon_1} \times \mathbf{a}_z \hat{\tilde{\Gamma}}_{te} e^{-j\tilde{\mathbf{k}}_r \cdot \mathbf{r}}. \tag{76}$$

The total field in the second medium is given by the transmitted field. The transmitted electric field is

$$\hat{\mathbf{E}}^t = -\frac{\mathbf{K}^t}{\Omega \epsilon_2} \times \mathbf{a}_z \hat{\tilde{T}}_{te} e^{-j\tilde{\mathbf{k}}_2 \cdot \mathbf{r}}. \tag{77}$$

The vectors $\mathbf{K}^i$, $\mathbf{K}^r$, and $\mathbf{K}^t$ are given by (K_{1x}, K_y) $(-K_{1x}, K_y)$, and (K_{2x}, K_y), respectively. Because the tangential phase is the same for all the fields, it is also true that K_y is the same for all the fields.

Note that only E_y nodes are present at the interface. Nevertheless, as in the continuous world, the tangential electric field must match at the interface, i.e.,

$$\mathbf{a}_y \cdot \hat{\mathbf{E}}_1 \Big|_{x=0} = \mathbf{a}_y \cdot \hat{\mathbf{E}}^t \Big|_{x=0}. \tag{78}$$

Expanding these terms yields

$$\frac{K_{1x}}{\Omega\epsilon_1}e^{-j\tilde{k}_1\sin(\phi_i)y} + \frac{K_{1x}}{\Omega\epsilon_1}\hat{\tilde{\Gamma}}_{te}e^{-j\tilde{k}_1\sin(\phi_i)y} =$$
$$\frac{K_{2x}}{\Omega\epsilon_2}\hat{\tilde{T}}_{te}e^{-j\tilde{k}_2\sin(\phi_t)y}. \tag{79}$$

Because the phase must match along the boundary, the complex exponential can be eliminated. Canceling Ω this equation can be written

$$1 + \hat{\tilde{\Gamma}}_{te} = \frac{\epsilon_1}{\epsilon_2}\frac{K_{2x}}{K_{1x}}\hat{\tilde{T}}_{te}. \tag{80}$$

Another equation relating the reflection and transmission coefficients can be obtained from the update-equation for the electric-field nodes on the interface. The relevant equation is the y component of Ampere's law evaluated at $x = 0$. This was given in (66) but that assumed propagation in a homogeneous space which is no longer pertinent. Instead, we explicitly write the spatial finite difference:

$$\begin{aligned}
j\Omega\epsilon_a\hat{E}_y\Big|_{x=0} &= -\tilde{\partial}_x\hat{H}_z\Big|_{x=0} \\
&= -\frac{1}{\delta}\left(\hat{H}_z^t\Big|_{x=\delta/2} - \hat{H}_{1z}\Big|_{x=-\delta/2}\right). \tag{81}
\end{aligned}$$

Unlike before, the spatial finite difference operator $\tilde{\partial}_x$ cannot be expressed directly in terms of K's since the difference involves fields on either side of the interface. The electric field in (81) can be represented as either the transmitted field or the sum of the incoming and reflected fields—the same result will ultimately be obtained. Using the transmitted field for the electric field and discarding common phase terms yields

$$j\Omega\epsilon_a\frac{K_{2x}}{\Omega\epsilon_2}\hat{\tilde{T}}_{te} = -\frac{1}{\delta}\left(\hat{\tilde{T}}_{te}e^{-j\kappa_{2x}} - \left[e^{j\kappa_{1x}} - \hat{\tilde{\Gamma}}_{te}e^{-j\kappa_{1x}}\right]\right), \tag{82}$$

where

$$\kappa_{1x} = \frac{\tilde{k}_1\cos(\phi_i)\delta}{2}, \tag{83}$$

$$\kappa_{2x} = \frac{\tilde{k}_2\cos(\phi_t)\delta}{2}. \tag{84}$$

Combining (80) and (82) and solving for the reflection coefficient yields

$$\hat{\tilde{\Gamma}}_{te} = \frac{\frac{K_{2x}}{\epsilon_2}e^{j\kappa_{1x}} - \frac{K_{1x}}{\epsilon_1}e^{-j\kappa_{2x}} - j\frac{\epsilon_a}{\epsilon_1\epsilon_2}K_{1x}K_{2x}\delta}{\frac{K_{2x}}{\epsilon_2}e^{-j\kappa_{1x}} + \frac{K_{1x}}{\epsilon_1}e^{-j\kappa_{2x}} + j\frac{\epsilon_a}{\epsilon_1\epsilon_2}K_{1x}K_{2x}\delta}. \tag{85}$$

As the discretization goes to zero, the third term in the numerator and denominator goes to zero, the complex exponentials approach one, and the K_x's approach the x component of the wavenumber in their respective media. Thus this expression gives the continuous-world reflection coefficient as

23

the discretization goes to zero. It is interesting to note that this is true even though at this point we have placed no restrictions on ϵ_a, the permittivity used for the nodes along the interface (although inherent in the derivation is the restriction that ϵ_a cannot be a pathological value such as zero).

Using (80) in (85), the transmission coefficient is found to be

$$\hat{\tilde{T}}_{te} = \frac{2\frac{K_{1x}}{\epsilon_1}\cos(\kappa_{1x})}{\frac{K_{2x}}{\epsilon_2}e^{-j\kappa_{1x}} + \frac{K_{1x}}{\epsilon_1}e^{-j\kappa_{2x}} + j\frac{\epsilon_a}{\epsilon_1\epsilon_2}K_{1x}K_{2x}\delta}. \tag{86}$$

Using Euler's formula to expand the complex exponentials and writing the K's in terms of sines, the reflection coefficient can be written

$$\hat{\tilde{\Gamma}}_{te} = \frac{\frac{\sin(\kappa_{x2})\cos(\kappa_{x1})}{\epsilon_2} - \frac{\sin(\kappa_{x1})\cos(\kappa_{x2})}{\epsilon_1} - j\aleph}{\frac{\sin(\kappa_{x2})\cos(\kappa_{x1})}{\epsilon_2} + \frac{\sin(\kappa_{x1})\cos(\kappa_{x2})}{\epsilon_1} + j\aleph} \tag{87}$$

where the imaginary term in the numerator and denominator is

$$\aleph = \frac{\sin(\kappa_{x1})\sin(\kappa_{x2})}{\epsilon_1\epsilon_2}(2\epsilon_a - \epsilon_1 - \epsilon_2). \tag{88}$$

Note that when ϵ_a is the average of the permittivities to either side of the interface $\aleph$ is zero. In this way the imaginary part of the reflection and transmission coefficients is zero. Since the continuous-world reflection and transmission coefficients are purely real, the imaginary part is an inherent error. The expressions above effectively constitute a proof that using the average permittivity for the interface nodes is optimum. For $\epsilon_a = (\epsilon_1 + \epsilon_2)/2$ the reflection and transmission coefficients become

$$\hat{\tilde{\Gamma}}_{te} = \frac{\epsilon_1\sin(\kappa_{x2})\cos(\kappa_{x1}) - \epsilon_2\sin(\kappa_{x1})\cos(\kappa_{x2})}{\epsilon_1\sin(\kappa_{x2})\cos(\kappa_{x1}) + \epsilon_2\sin(\kappa_{x1})\cos(\kappa_{x2})}, \tag{89}$$

$$\hat{\tilde{T}}_{te} = \frac{2\epsilon_2\sin(\kappa_{x1})\cos(\kappa_{x1})}{\epsilon_1\sin(\kappa_{x2})\cos(\kappa_{x1}) + \epsilon_2\sin(\kappa_{x1})\cos(\kappa_{x2})}. \tag{90}$$

Despite the change in permeability, these equations are seemingly independent of permeability. However, the permeabilities dictate the wave numbers in the different media and hence the permeabilities are implicitly contained within these equations.

Reflection and transmission coefficients for this polarization were provided in [4] (ref. (72) and (73) of that paper). The reflection coefficient in that work involves the sum of 28 terms (these terms involve the product of a total of 17 complex exponentials and 30 sine functions) and was obtained with the aid of a computer algebra package. The complexity of that expression is, it must be noted, a consequence of Moss *et al.* considering more complex media than that assumed here. However, their final results do tend to obscure the simplicity which pertains to the problem of interest here. The reflection coefficients which pertain to PML interfaces have also been studied extensively. Derivations of the numeric PML reflection coefficient can be found in [18–21].

With the reflection and transmission coefficients known, the incident field can be calculated at an arbitrary point given the source function $f[q]$ at a reference point and the direction of propagation of the incident field. The location of the reference point is unchanged from that depicted in

24

Fig. 4. Here we take the "incident field" to mean the sum of the incoming and reflected field if a node is to the left of the interface and the transmitted field if the node is to the right. Thus, the time-domain incident magnetic field for points to the left of the interface are given by

$$H_{1z}\left[m+\frac{1}{2}, n+\frac{1}{2}, q+\frac{1}{2}\right] =$$
$$\mathcal{F}^{-1}\left[F(\omega)\left(e^{-j\tilde{\mathbf{k}}_i \cdot \mathbf{r}} - \hat{\tilde{\Gamma}}_{te} e^{-j\tilde{\mathbf{k}}_r \cdot \mathbf{r}}\right)\right], \tag{91}$$

where $F(\omega) = \mathcal{F}[f[q]]$. As discussed in connection with (56), the offsets of $1/2$ are accounted for in the inverse transforms. From (67) and (68), the x and y components of the electric field are

$$E_{1x}\left[m+\frac{1}{2}, n, q\right] =$$
$$-\mathcal{F}^{-1}\left[\frac{K_y F(\omega)}{\Omega \epsilon_1}\left(e^{-j\tilde{\mathbf{k}}_i \cdot \mathbf{r}} - \hat{\tilde{\Gamma}}_{te} e^{-j\tilde{\mathbf{k}}_r \cdot \mathbf{r}}\right)\right], \tag{92}$$

$$E_{1y}\left[m, n+\frac{1}{2}, q\right] =$$
$$\mathcal{F}^{-1}\left[\frac{K_x F(\omega)}{\Omega \epsilon_1}\left(e^{-j\tilde{\mathbf{k}}_i \cdot \mathbf{r}} + \hat{\tilde{\Gamma}}_{te} e^{-j\tilde{\mathbf{k}}_r \cdot \mathbf{r}}\right)\right]. \tag{93}$$

These expressions, as well as the corresponding expression for the transmitted fields, are evaluated for the points adjacent to the TFSF boundary.

To illustrate the behavior of the TFSF boundary, Fig. 7 shows two snapshots of the magnetic field in a computational domain which is 180 by 200 cells. Free space is to the left and extends over 90 cells. To the right is a dielectric with a permittivity of $4\epsilon_0$ (E_y nodes along the interface use a permittivity of $2.5\epsilon_0$). The permeability in both regions is that of free space. This is equivalent to an acoustic simulation in which the sound speed in the second medium is half that of the first. The incoming pulse is a Ricker wavelet discretized such that there are 20 cells per free-space wavelength at the most energetic frequency. This corresponds to 10 cells per wavelength in the dielectric. The SF region is 15 cells thick, the incident angle is 60 degrees, and the Courant number is $0.95/\sqrt{3}$.

Figure 7(a) shows the H_z field at 150 time steps when the leading edge of the pulse has first encountered the dielectric at the center of the bottom of the figure. Figure 7(b) shows the field at 350 time steps. Now the reflected and transmitted field are clearly evident. Since no scatterer is present in this simulation, no scattered fields are visible in the SF region (the plot uses three decades of logarithmic scaling). One can clearly see the refraction of the transmitted field. Also, owing to the higher permittivity of the second medium, the transmitted field suffers more numeric dispersion than fields in the first medium. (Dispersion in the FDTD grid is dictated by the discretization [2]. The higher permittivity in the second medium results in shorter wavelengths, and hence coarser discretization and greater dispersion, than in the first medium.) The increased dispersion causes the transmitted pulse to broaden noticeably as it propagates—one can see that the pulse is thinest at the interface. One may ask why, at any given time step, the incoming way does not have a similar appearance to the transmitted field, i.e., thinner to the left and thicker to the right? The
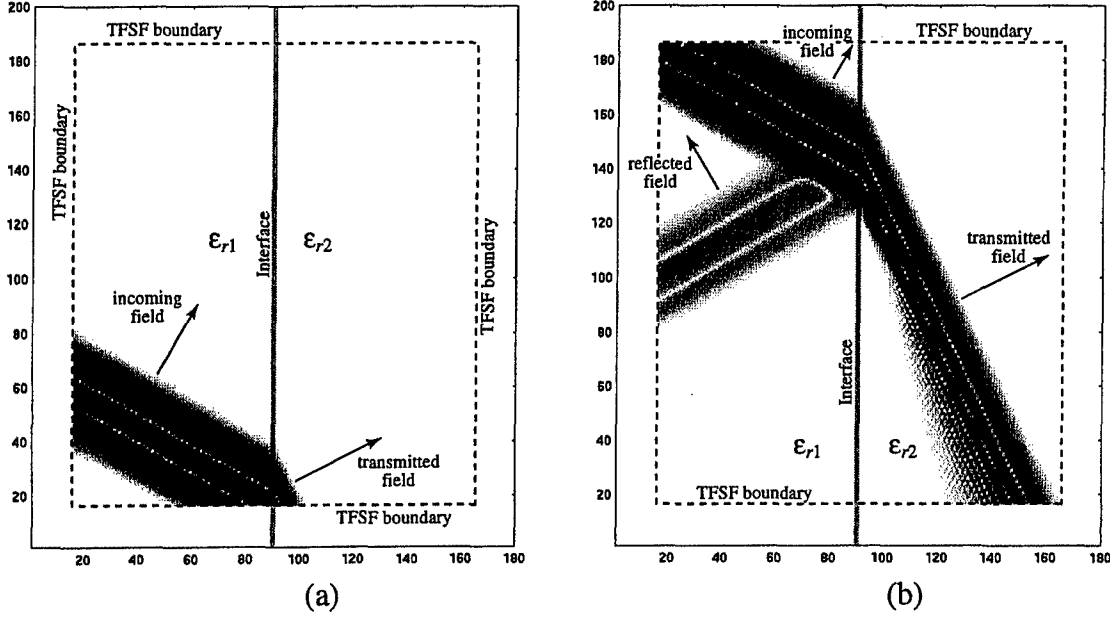
Figure 7: Snapshots of the magnetic field at time-steps (a) 150 and (b) 350. This is equivalent to snapshots of the pressure in a fluid-fluid problem where the sound speed in the second medium is half of that in the first medium

answer is that the incident field along the TFSF boundary is exactly matching the phase speed for all the spectral components for the particular incident angle, i.e., all spectral components have the same ϕ_i. At the interface between free space and the dielectric, boundary conditions dictate the fields must be continuous. However, the free-space phase speeds are not matched to the phase speeds in the dielectric so as to yield a single transmitted angle. Since the phase speeds are a function of the frequency, this causes the depth-dependent broadening (or thought of another way, the frequency-dependent refraction where ϕ_t is a function of frequency).

As with the PEC simulation, the leaked fields are approximately 100 dB down from the peak interior fields. When a more reasonable discretization is used (i.e., there is not significant energy with discretizations less than 10 cells per wavelength in the second medium), the peak leaked fields are more than 180 dB down from the peak of the incident field.

6 TM^z Polarization with a Dielectric Halfspace

Consider the TM^z grid shown in Fig. 8. For this polarization the electric field can be equated with pressure and the magnetic field can be equated with the velocity. The interface is aligned with H_x and E_z nodes. The arrangement and indexing of nodes is consistent with the TE^z grid in that both grids could be considered slices of a 3D grid where magnetic-field nodes are centered on the faces of the Yee cube while electric-field nodes are centered on the edges. For this polarization both electric- and magnetic-field nodes lie on the interface. The permittivity and permeability associated with these nodes is ϵ_a and μ_a, respectively, which are left arbitrary for now. We again wish to find the reflection and transmission coefficients. The incoming, reflected, and transmitted
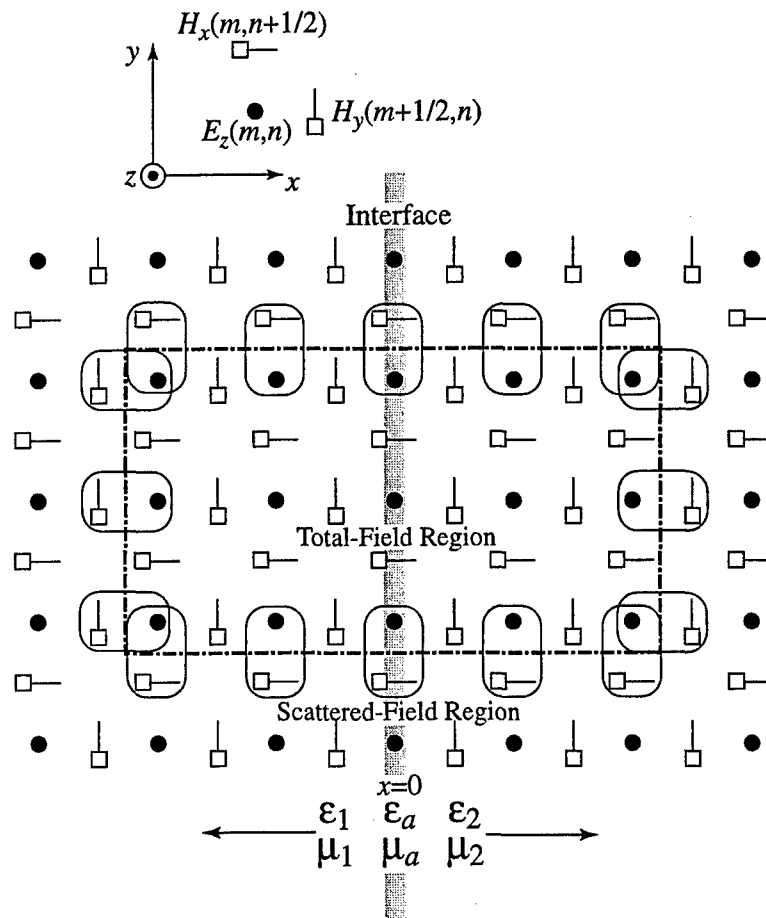
26

Figure 8: Depiction of a TM^z grid with two dielectric halfspaces. This is equivalent to an acoustic simulation where the electric field can be equated with pressure and the magnetic field nodes can be equated with the components of the velocity vector.

electric field are given by, respectively,

$$\hat{\mathbf{E}}^i = \mathbf{a}_z e^{-j\tilde{\mathbf{k}}_i \cdot \mathbf{r}}, \tag{94}$$

$$\hat{\mathbf{E}}^r = \mathbf{a}_z \hat{\tilde{\Gamma}}_{tm} e^{-j\tilde{\mathbf{k}}_r \cdot \mathbf{r}}, \tag{95}$$

$$\hat{\mathbf{E}}^t = \mathbf{a}_z \hat{\tilde{T}}_{tm} e^{-j\tilde{\mathbf{k}}_t \cdot \mathbf{r}}. \tag{96}$$

where $\hat{\tilde{\Gamma}}_{tm}$ and $\hat{\tilde{T}}_{tm}$ are the TM^z reflection and transmission coefficients, respectively. Temporal dependence is given by $\exp(j\omega q\Delta_t)$ and is common to all terms (hence it is not shown explicitly). The definitions of other terms are as before. The FDTD form of Ampere's law is

$$j\Omega\epsilon\hat{E}_z = \tilde{\partial}_x \hat{H}_y - \tilde{\partial}_y \hat{H}_x. \tag{97}$$

Because, for the assumed geometry, the phase dependence in the y direction is the same throughout the grid, $\tilde{\partial}_y$ can be replaced with $-jK_y$. For any of the fields, the FDTD form of Faraday's relates the electric and magnetic fields via

$$-j\Omega\hat{\mathbf{H}} = -j\mathbf{K} \times \hat{\mathbf{E}} = -\mathbf{a}_x jK_y\hat{E}_z + \mathbf{a}_y jK_x\hat{E}_z \tag{98}$$

so that the magnetic field components are given by

$$\hat{H}_x = \frac{K_y}{\mu\Omega}\hat{E}_z, \tag{99}$$

$$\hat{H}_y = -\frac{K_x}{\mu\Omega}\hat{E}_z. \tag{100}$$

As before, K_x has equal amplitude but opposite sign for the incoming and reflected waves.

Matching the z component of the electric field at the interface dictates that the sum of the incoming and reflected fields must equal the transmitted field at $x = 0$. Since the phase must be equal along the boundary this reduces to

$$1 + \hat{\tilde{\Gamma}}_{tm} = \hat{\tilde{T}}_{tm}. \tag{101}$$

The other equation relating the reflection and transmission coefficients is obtained from Ampere's law applied to the nodes on the interface. Using (99) in (97) and rearranging yields

$$j\left(\Omega\epsilon_a - \frac{K_y^2}{\Omega\mu_a}\right)\hat{E}_z\bigg|_{x=0} = \tilde{\partial}_x\hat{H}_y\bigg|_{x=0} \tag{102}$$

$$= \frac{1}{\delta}\left(\hat{H}_y^t\bigg|_{x=\delta/2} - \hat{H}_{1y}\bigg|_{x=-\delta/2}\right) \tag{103}$$

where $\hat{H}_{1y}$ is the y component of the sum of the incoming and reflected waves and $\hat{H}_y^t$ is the y component of the transmitted field. After using (100) to express $\hat{H}_y$ in terms of $\hat{E}_z$ and discarding common phase terms, (103) yields

$$j\delta\left(\Omega^2\mu_a\epsilon_a - K_y^2\right)\hat{\tilde{T}}_{tm} =$$
$$-\frac{\mu_a}{\mu_2}K_{2x}\hat{\tilde{T}}_{tm}e^{-j\kappa_{2x}} + \frac{\mu_a}{\mu_1}K_{2x}\left(e^{j\kappa_{1x}} - \hat{\tilde{\Gamma}}_{tm}e^{-j\kappa_{1x}}\right) \tag{104}$$

28

where the κ's are defined in (83) and (84).

Using (101) and (104) to solve for the reflection coefficient yields

$$\hat{\hat{\Gamma}}_{tm} = \frac{\frac{\mu_a}{\mu_1} K_{1x} e^{j\kappa_{1x}} - \frac{\mu_a}{\mu_2} K_{2x} e^{-j\kappa_{2x}} - j\delta \left(\Omega^2 \mu_a \epsilon_a - K_y^2\right)}{\frac{\mu_a}{\mu_1} K_{1x} e^{-j\kappa_{1x}} + \frac{\mu_a}{\mu_2} K_{2x} e^{-j\kappa_{2x}} + j\delta \left(\Omega^2 \mu_a \epsilon_a - K_y^2\right)}. \tag{105}$$

This can be compared to (45) of [4] which appears to have a typographical error. (The exponent of the first term in the numerator has the wrong sign. Also the term K_z [with no numeric subscript] which appears in that expression is never explicitly defined.) The transmission coefficient is

$$\hat{\hat{T}}_{tm} = \frac{2\frac{\mu_a}{\mu_1} K_{1x} \cos(\kappa_{1x})}{\frac{\mu_a}{\mu_1} K_{1x} e^{-j\kappa_{1x}} + \frac{\mu_a}{\mu_2} K_{2x} e^{-j\kappa_{2x}} + j\delta \left(\Omega^2 \mu_a \epsilon_a - K_y^2\right)}. \tag{106}$$

When, as was used in the TE^z case, ϵ_a is the average of the permittivity to either side of the interface, one can write

$$\delta(\Omega^2 \mu_a \epsilon_a - K_y^2) = \frac{\delta}{2} \left(\Omega^2 \mu_a \epsilon_1 + \Omega^2 \mu_a \epsilon_2 - 2K_y^2\right) \tag{107}$$

Assuming the permeability μ_a is the harmonic mean of the permeabilities to either side of the interface, i.e., $\mu_a = 2\mu_1\mu_2/(\mu_1 + \mu_2)$, the right-hand side of (107) can be written

$$\frac{\delta}{2} \left(\frac{2\mu_2}{\mu_1 + \mu_2}(\Omega^2 \mu_1 \epsilon_1 - K_y^2) + \frac{2\mu_1}{\mu_1 + \mu_2}(\Omega^2 \mu_2 \epsilon_2 - K_y^2)\right). \tag{108}$$

Using the dispersion relation (65), this becomes

$$\frac{\delta\mu_2}{\mu_1 + \mu_2} K_{1x}^2 + \frac{\delta\mu_1}{\mu_1 + \mu_2} K_{2x}^2. \tag{109}$$

Employing the definition of the K's (63), allows us to write this imaginary term as

$$\frac{4\mu_2}{\delta(\mu_1 + \mu_2)} \sin^2(\kappa_{1x}) + \frac{4\mu_1}{\delta(\mu_1 + \mu_2)} \sin^2(\kappa_{2x}). \tag{110}$$

This final form is convenient because, assuming $\epsilon_a = (\epsilon_1 + \epsilon_2)/2$ and $\mu_a = 2\mu_1\mu_2/(\mu_1 + \mu_2)$, when the complex exponential in (105) and (106) are expanded it is clear that the imaginary part of that expansion identically cancels the term shown in (110). Thus, the resulting expressions are purely real and, after employing the double-angle formula, given by

$$\hat{\hat{\Gamma}}_{tm} = \frac{\mu_2 \sin(2\kappa_{1x}) - \mu_1 \sin(2\kappa_{2x})}{\mu_2 \sin(2\kappa_{1x}) + \mu_1 \sin(2\kappa_{2x})}, \tag{111}$$

$$\hat{\hat{T}}_{tm} = \frac{2\mu_2 \sin(2\kappa_{1x})}{\mu_1 \sin(2\kappa_{1x}) + \mu_2 \sin(2\kappa_{2x})}. \tag{112}$$

These expressions reduce to that of the continuous world when the discretization goes to zero. Since the exact expressions are purely real, this serves as proof of the optimality of using the arithmetic mean for the interface permittivity and the harmonic mean for the permeability.

Implementation of an AFP TFSF boundary for the TM^z polarization also yields leaked fields which are approximately 100 dB down from the peak field when the incoming field is very coarsely discretized. Using a discretization which is typical of actual practice, the leaked field obtains a maximum of approximately -180 dB relative to the peak of the incoming field.

29

7 Lossy Materials

This section discusses the construction of a TFSF boundary which pertains to the case of a plane wave (identified as the incoming wave) obliquely incident on a lossy halfspace. Although not strictly required, the incoming wave is assumed to travel in a lossless medium. As before, the boundary between the two media is assumed to be planar insofar as the calculation of the incident field is concerned.

As has been discussed, the AFP TFSF boundary requires that one be able to calculate analytically the incident field at an arbitrary point. This necessitates calculation of the numeric wavenumbers as well as the numeric reflection and transmission coefficients. (Note that for any particular simulation the interface between the media need not be planar and the contents of the TF region are arbitrary. The assumption of homogeneous halfspaces and a planar interface are germane only to the calculation of the incident field.) We start by describing the equations which govern FDTD propagation in lossy medium.

Consider a harmonic field polarized in the z direction propagating in the xy plane of an FDTD grid, i.e., TM^z polarization. The electric and magnetic fields can be written

$$
\begin{aligned}
\mathbf{a}_z \hat{E}_z &= \mathbf{a}_z \hat{E}_0 e^{-j(\tilde{k}_x m\delta + \tilde{k}_y n\delta)} e^{j\omega q\Delta_t} \\
&= \mathbf{a}_z \hat{E}_0 e^{-j\tilde{\mathbf{k}}\cdot\mathbf{r}} e^{j\omega q\Delta_t},
\end{aligned}
\tag{113}
$$

$$
\begin{aligned}
\hat{\mathbf{H}} &= \mathbf{a}_x \hat{H}_x + \mathbf{a}_y \hat{H}_y = (\mathbf{a}_x \hat{H}_{0x} + \mathbf{a}_y \hat{H}_{0y}) e^{-j\tilde{\mathbf{k}}\cdot\mathbf{r}} e^{j\omega q\Delta_t}, \\
&= \hat{\mathbf{H}}_0 e^{-j\tilde{\mathbf{k}}\cdot\mathbf{r}} e^{j\omega q\Delta_t}.
\end{aligned}
\tag{114}
$$

where δ is the spatial step size (assumed uniform for the sake of notational simplicity), Δ_t is the temporal step size, (m, n) are the spatial indices in the x and y directions, respectively, q is the temporal index, ω is the frequency, $\tilde{\mathbf{k}} = \mathbf{a}_x \tilde{k}_x + \mathbf{a}_y \tilde{k}_y$ is the wave vector, $\mathbf{r} = \mathbf{a}_x m\delta + \mathbf{a}_y n\delta$ is the position vector, and $\hat{E}_0$ is an arbitrary amplitude. A tilde is used to indicate a numeric quantity, i.e., one whose value in the FDTD grid differs from that in the continuous world. The amplitudes $\hat{H}_{0x}$ and $\hat{H}_{0y}$ are dictated by the impedance of the grid.

Discretizing time, Ampere's law expanded about the time-step $q + 1/2$ is

$$
\nabla \times \mathbf{H}^{q+1/2} = \epsilon \frac{\mathbf{E}^{q+1} - \mathbf{E}^q}{\Delta_t} + \sigma \frac{\mathbf{E}^{q+1} + \mathbf{E}^q}{2},
\tag{115}
$$

where the superscript indicates the time step, σ is the conductivity, ϵ is the permittivity, and time-averaging is used to obtain the conduction current at the necessary temporal location. For the given harmonic fields, the temporal finite difference can be expressed as

$$
j\frac{2}{\Delta_t} \sin\left(\frac{\omega\Delta_t}{2}\right) \hat{\mathbf{E}}^{q+1/2} = j\Omega \hat{\mathbf{E}}^{q+1/2},
\tag{116}
$$

whereas the time-average term can be written

$$
\cos\left(\frac{\omega\Delta_t}{2}\right) \hat{\mathbf{E}}^{q+1/2} = A\hat{\mathbf{E}}^{q+1/2}.
\tag{117}
$$

30

The discretized form of the curl operation is unchanged from that presented in [5]. For a harmonic field, the finite differences in the x and y directions, identified as $\tilde{\partial}_x$ and $\tilde{\partial}_y$, respectively, can be represented by multiplicative operators, i.e.,

$$\tilde{\partial}_\xi = -j\frac{2}{\delta}\sin\left(\frac{\tilde{k}_\xi\delta}{2}\right) = -jK_\xi \tag{118}$$

where $\xi \in \{x, y\}$. Thus Ampere's law can be written

$$-jK_x\hat{H}_{0y} + jK_y\hat{H}_{0x} = (j\epsilon\Omega + \sigma A)\hat{E}_0 = j\epsilon\Omega\left[1 - j\frac{\sigma A}{\epsilon\Omega}\right]\hat{E}_0. \tag{119}$$

The phase term $e^{j\omega(q+1/2)\Delta_t}$ was common to all terms and hence dropped.

Defining $\mathbf{K} = \mathbf{a}_x K_x + \mathbf{a}_y K_y$, the discrete form of Faraday's law can be written

$$-j\mathbf{K} \times \hat{\mathbf{E}}^q = -j\mu\Omega\hat{\mathbf{H}}^q \tag{120}$$

where μ is the permeability (it is assumed the magnetic conductivity is zero although this is not required). This yields two equations

$$\hat{H}_{x0} = \frac{K_y}{\mu\Omega}\hat{E}_0, \tag{121}$$

$$\hat{H}_{y0} = -\frac{K_x}{\mu\Omega}\hat{E}_0. \tag{122}$$

Using (121) and (122) in (119), one obtains the dispersion equation for lossy media

$$K_x^2 + K_y^2 = \Omega^2\mu\epsilon\left[1 - j\frac{\sigma A}{\epsilon\Omega}\right] \tag{123}$$

This is the dispersion relationship for lossy material which was previously considered in [22] and more recently studied in [23]. We define the complex permittivity to be

$$\hat{\epsilon} = \epsilon\left[1 - j\frac{\sigma A}{\epsilon\Omega}\right], \tag{124}$$

$$= \epsilon\left[1 - jL_\sigma\cot\left(\frac{\omega\Delta_t}{2}\right)\right], \tag{125}$$

where the loss-factor L_σ is defined as $\sigma\Delta_t/(2\epsilon)$, the real quantity ϵ is given by $\epsilon_0\epsilon_r$ and ϵ_0 is the permittivity of free space. Expressed in terms of the underlying functions the dispersion relation is

$$\sin^2(\kappa_x) + \sin^2(\kappa_y) = \frac{\mu_r\epsilon_r}{S_c^2}\sin^2\left(\frac{\omega\Delta_t}{2}\right)\left[1 - jL_\sigma\cot\left(\frac{\omega\Delta_t}{2}\right)\right], \tag{126}$$

where κ_ξ is $\tilde{k}_\xi\delta/2$ and $\xi \in \{x, y\}$.

In the construction of the AFP TFSF boundary the frequency and the wave vector components in the first medium can be easily calculated. Due to phase matching along the boundary, the

31

tangential component of the wave number must be the same in both media, i.e., $\tilde{k}_{y2} = \tilde{k}_{y1}$ when the interface corresponds to a constant x plane. We ignore superluminal wave numbers and hence $\tilde{k}_{y2}$ is purely real. (Throughout the analysis we ignore superluminal propagation which is inherently present but of little practical concern. See [9, 13] for further details.) Since the frequency is know, the only unknown in (126) is $\hat{\tilde{k}}_x$, the normal component of the wavenumber which is complex due to the loss. We separate the real and imaginary parts of $\hat{\tilde{k}}_x$ as $\hat{\tilde{k}}_x = \tilde{k}'_x + j\tilde{k}''_x$ or, correspondingly, $\hat{\tilde{k}}_x \delta/2 = \hat{\kappa}_x = \kappa'_x + j\kappa''_x$. Plugging this into (126), expanding terms, and separating real and imaginary parts yields

$$\cos(\kappa'_x)\cosh(\kappa''_x) = C', \tag{127}$$

$$\sin(\kappa'_x)\sinh(\kappa''_x) = C'', \tag{128}$$

where

$$C' = 1 + 2\left[\sin^2(\kappa_y) - \frac{\mu_r \epsilon_r}{S_c^2}\sin^2\left(\frac{\omega \Delta_t}{2}\right)\right], \tag{129}$$

$$C'' = -\frac{\mu_r \epsilon_r}{S_c^2} L_\sigma \sin(\omega \Delta_t). \tag{130}$$

Solving (127) and (128) for κ'_x and κ''_x (and using physical arguments to eliminate non-physical solutions) yields

$$\kappa'_x = \frac{1}{2}\cos^{-1}\left[\frac{UV}{\sqrt{8C'}}\right], \tag{131}$$

$$\kappa''_x = -\frac{1}{2}\cosh^{-1}\left[\frac{U}{\sqrt{2}}\right], \tag{132}$$

where

$$U = \left(M + \sqrt{(M - 2C')(M + 2C')}\right)^{1/2}, \tag{133}$$

$$V = M - \sqrt{(M - 2C')(M + 2C')}, \tag{134}$$

$$M = 1 + C'^2 + C''^2. \tag{135}$$

The numeric reflection and transmission coefficients for TM^z polarization were presented in (111) and (112) for lossless isotropic media and in [4] for uniaxial media. We assume an interface which is aligned with the E_z and H_x nodes as shown in Fig. 9. The FDTD reflection and transmission coefficients which were derived already still pertain to the lossy case—the only difference is that the permittivity and wavenumber in the second medium become complex. When the electric-field nodes on the interface use the arithmetic average of the values to either side for the conductivity and the real part of the permittivity while the magnetic-field nodes on the interface use the harmonic mean for the permeability (i.e., $\mu_a = 2\mu_1\mu_2/(\mu_1 + \mu_2)$), the reflection and transmission coefficients are, respectively,

$$\hat{\tilde{\Gamma}}_{tm} = \frac{\mu_2 \sin(2\kappa_{1x}) - \mu_1 \sin(2\hat{\kappa}_{2x})}{\mu_2 \sin(2\kappa_{1x}) + \mu_1 \sin(2\hat{\kappa}_{2x})}, \tag{136}$$

$$\hat{\tilde{T}}_{tm} = \frac{2\mu_2 \sin(2\kappa_{1x})}{\mu_1 \sin(2\kappa_{1x}) + \mu_2 \sin(2\hat{\kappa}_{2x})}. \tag{137}$$
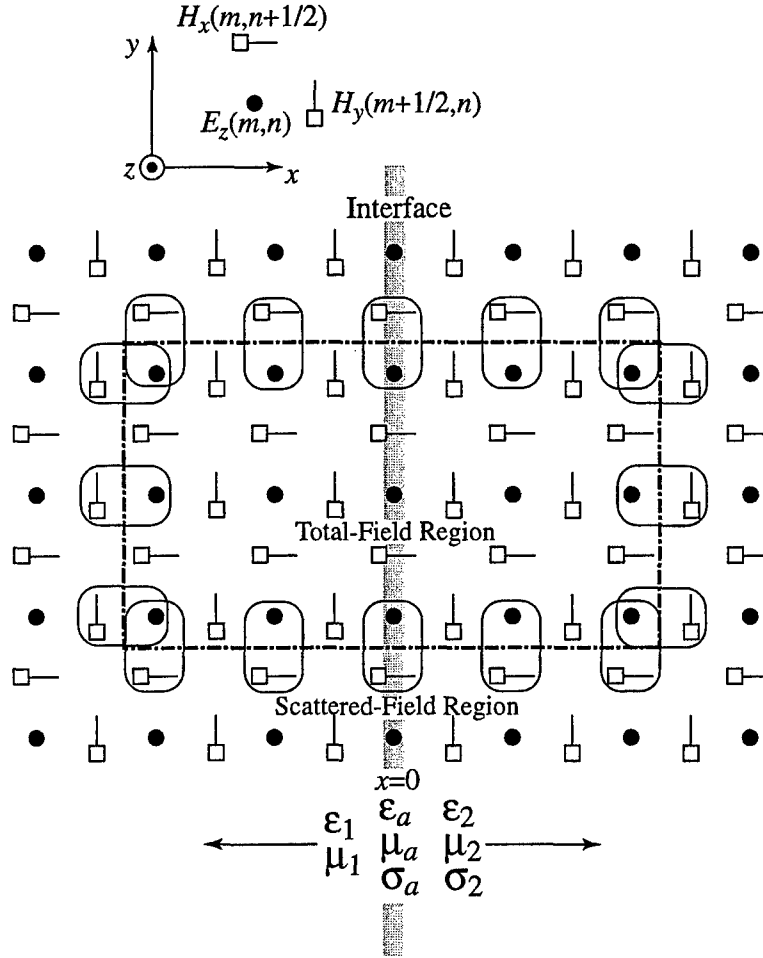
32

Figure 9: Depiction of a TM^z grid with two dielectric halfspaces. The interface, corresponding to $x = 0$, is aligned with E_z and H_x nodes. The second medium is assumed lossy. Along the interface the electric-field nodes use the arithmetic average of the permittivity and conductivity to either side while the magnetic-field nodes use the harmonic mean of the permeabilities. The dashed line represents the TFSF boundary. The nodes enclosed in rounded rectangles are tangential to the TFSF boundary and hence must have their updates corrected using the incident field associated with the other node in the box.

These values reduce to the continuous-world values in the limit as the discretization goes to zero. If one does not use the average material properties at the interface. This additional term can cause the agreement between the FDTD and continuous-world values to be better than when using averaging. However, this improvement only exists over a very narrow band of frequencies and the agreement is worse at all other frequencies. Hence we continue to assume that the mean values are used for the interface material parameters.

Although the dispersion relationship was derived in terms of TM^z polarization, the same results pertain to TE^z polarization, i.e., (131) and (132) still pertain. The reflection and transmission coefficients derived previously are still pertinent provided one allows the permittivity and wavenumber to be complex. The assumed TE^z grid is shown in Fig. 10. If the arithmetic mean is used for the conductivity and permittivity on the boundary, the reflection and transmission coefficients are essentially unchanged from before, i.e.,

$$\hat{\Gamma}_{te} = \frac{\epsilon_1 \sin(\hat{\kappa}_{x2}) \cos(\kappa_{x1}) - \hat{\epsilon}_2 \sin(\kappa_{x1}) \cos(\hat{\kappa}_{x2})}{\epsilon_1 \sin(\hat{\kappa}_{x2}) \cos(\kappa_{x1}) + \hat{\epsilon}_2 \sin(\kappa_{x1}) \cos(\hat{\kappa}_{x2})}, \tag{138}$$

$$\hat{T}_{te} = \frac{2\hat{\epsilon}_2 \sin(\kappa_{x1}) \cos(\kappa_{x1})}{\epsilon_1 \sin(\hat{\kappa}_{x2}) \cos(\kappa_{x1}) + \hat{\epsilon}_2 \sin(\kappa_{x1}) \cos(\hat{\kappa}_{x2})}. \tag{139}$$

Using the wavenumbers as well as the reflection and transmission coefficients described here, the implementation of the AFP TFSF boundary then follows the implementation described previously.

8 Incidence beyond the Critical Angle

By allowing the normal component of the wave number in the second medium to be complex, the capability is automatically present to model incoming fields which are incident beyond the critical angle, i.e., the fields are evanescent in the second medium. As discussed in [13], the critical angle in the FDTD world differs from that in the continuous world and is, in fact, a function of frequency. Nevertheless, we will refer to the critical angle as if it were a constant. (When the second material is lossy, the concept of a critical angle is nebulous since some energy is lost in the second medium. The code developed here handles both lossless and lossy material but this section will be limited to lossless material.)

When modeling incidence beyond the critical angle, one must keep in mind the somewhat unusual behavior of the incident field. The geometry assumed here is of an infinite, pulsed incoming plane wave propagating obliquely toward an infinite planar interface separating two half spaces in which the speed of propagation in the second medium is faster than in the first. Roughly speaking, fields in the second medium can, and will, move tangentially along the boundary faster than they can in the first medium. However, to satisfy the boundary conditions along the interface, these faster moving fields will couple energy back into the first medium. These fields will be in advance of the incoming wave. These "advanced fields," despite arriving at any given point before the incoming wave, are causal. A good discussion of these fields can be found in [24, 25].

In theory, the advanced fields are non-zero throughout space and this could be problematic for implementation of a TFSF boundary which assumes the fields are initially zero throughout
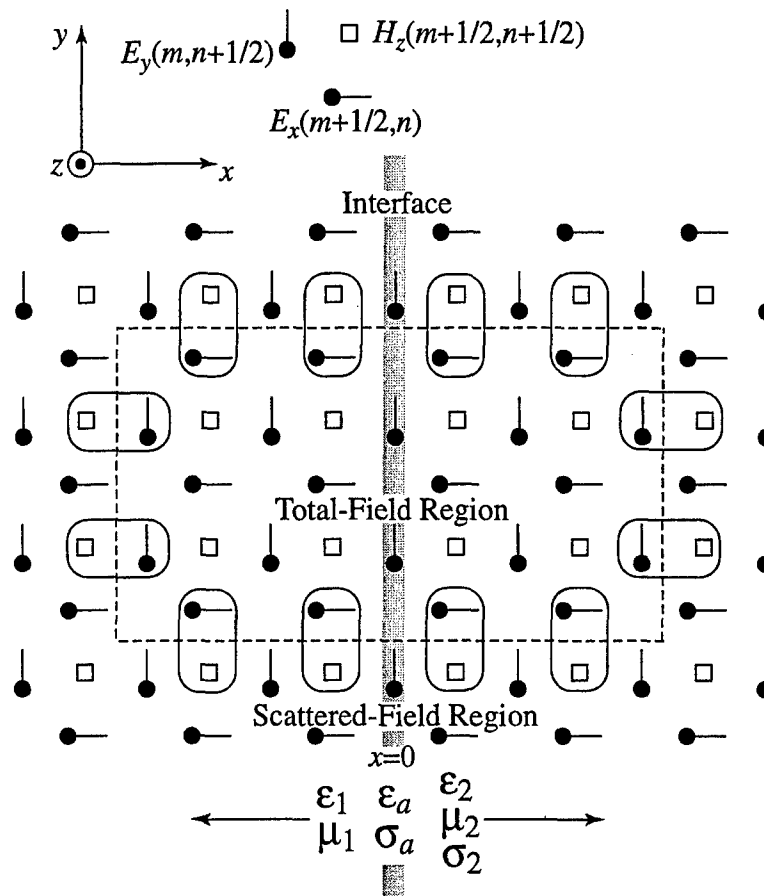
Figure 10: Depiction of a TE^z grid with two dielectric halfspaces, the second of which is lossy. The interface, corresponding to $x = 0$, is aligned with E_y nodes. For the interface nodes the conductivity and permittivity use the arithmetic mean of the values to either side.

the computational domain. However, in practice the advanced field are small and can be made arbitrarily small by delaying the incoming wave. Additionally, if there is loss present in the second medium, this serves to diminish the advanced fields.

Despite the existence of these advanced fields, the AFP TFSF implementation is oblivious to them—the same code can be used for all incident angles. To illustrate the case of incidence beyond the critical angle, Fig. 11 shows the magnitude of the H_z field in a TE^z simulation where $\mu_1 = \mu_2 = \mu_0$, $\epsilon_{r1} = 2$, $\epsilon_{r2} = 1$, the incident angle is 60 degrees, and the Courant number S_c is $1/\sqrt{2}$. The computational domain is 180×200 cells, the interface runs vertically through the middle of the grid, and the TFSF boundary is offset 15 cells from the edge for the grid. The incoming wave is a Ricker wavelet discretize such that there are 20 cells per wavelength (in the first medium) at the frequency with the greatest spectral content. The Ricker wavelet is broad-banded (see [5] for further details of this source function).

Figure 11(a) shows the field at time-step 180, shortly after the field has become clearly visible in the TF region. The incoming wave has unit peak amplitude and the images use logarithmic scaling so that fields are essentially visible over three decades (i.e., fields greater than 10^{-3} are visible). In Fig. 11(a) one can see the distinct incoming field as well as the "haze" associated with the field which arrives in advance of the incoming wave. This leading field exists throughout the computational domain but falls off as one moves away from the incoming wave.

Figures 11(b) and (c) show the field at time-steps 330 and 460, respectively. Note that the incident field is not visible in the SF region. For this particular simulation the peak leaked field is less than 6×10^{-5}. This is much greater than the leaked field found in the typical beneath-critical-angle case where the leaked field is on the order of 10^{-9} for reasonable discretizations. The amount of leaked field can be reduced further by delaying the incoming wave or by changing the source function so that it is has less low-frequency content. (Low-frequency energy, with its long wavelengths, falls off very slowly.) If loss can be added to the second medium, this can also significantly reduce the leaked field.

To verify that the observed leaked fields were a consequence of the inherent nature of the incident field and not the result of a coding error, a simulation was performed in which the AFP technique was used to calculate the initial field at every point within the TF region. In this case the leaked field dropped to approximately 10^{-15}. Thus the implementation was correct and the leaked fields are a consequence of the AFP calculation yielding a particular non-zero value over the entire TFSF boundary but the TF region is initially zero. Unfortunately this type of initialization is not a practical way to lower the leaked field for two reasons. First, it is computationally cumbersome and, second, it presupposes no scatterers are present in the TF region. (Simulations which lack a scatterer are of no practical interest.)

Figure 11(d) is also a snapshot at time-step 460. However, to illustrate that the contents of the TF region can be arbitrary, a notch has been placed in the interface. The notch is 20×20 cells where the second medium now protrudes into the first. Because of this notch the fields in the second medium are no longer purely evanescent. One can see the field scattered by the notch and how it has passed into the SF region at this particular time step.
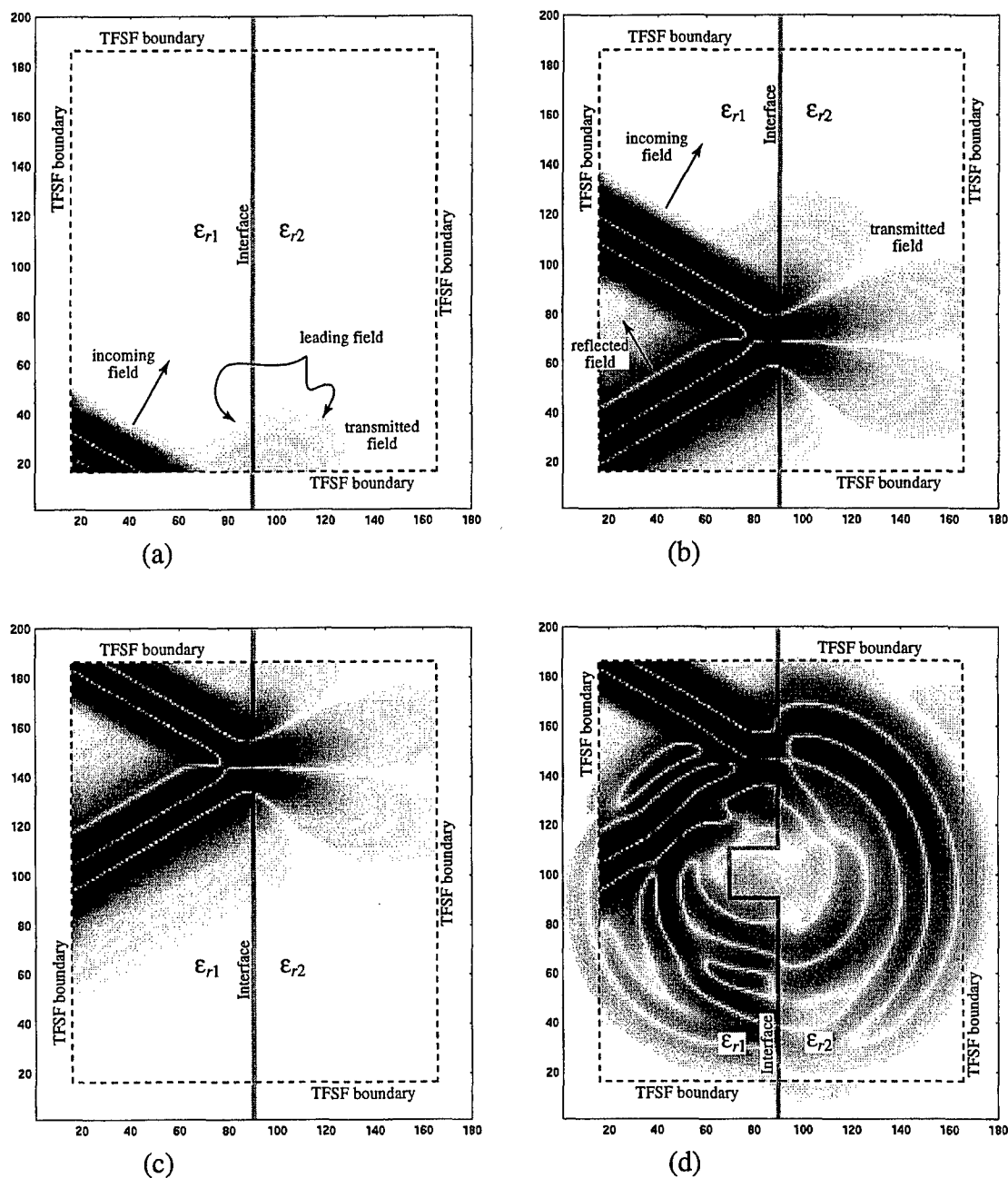
Figure 11: Snapshots of the magnetic field at time-steps (a) 180, (b) 330 and (c) 460. (d) Magnetic field at time-step 460 showing the field scattered from a notch in the surface. The incident angle is 60 degrees with respect to horizontal.
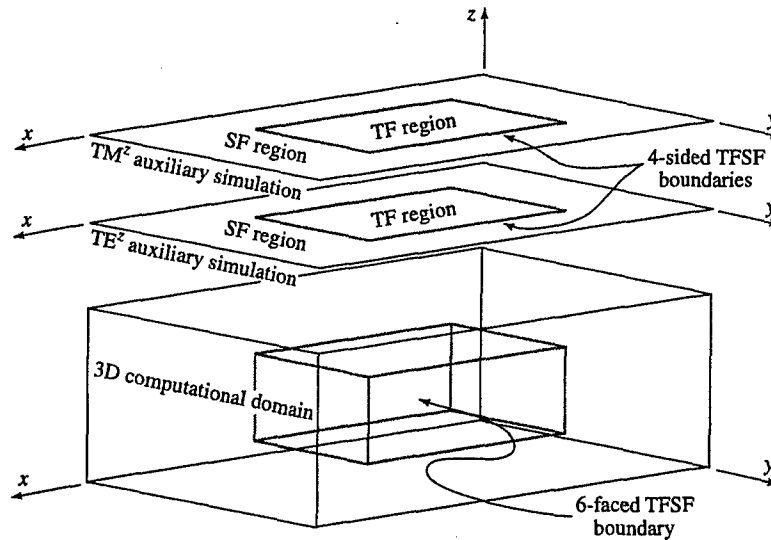
37

Figure 12: Depiction of 3D computational domain with associated 2D auxiliary simulations.

9 Three-Dimensional Simulations

At present the AFP TFSF method cannot be applied to three-dimensional (3D) halfspace problems with arbitrary incidence because the numeric reflection and transmission coefficients have not been obtained for the general 3D case. Were these available, the 3D formulation of the AFP TFSF technique would be a trivial extension to the two-dimensional (2D) case. One would merely have three components to the wave vector instead of two and evaluation points would have three indices instead of two. However, precomputing the incident field over the TFSF boundary in 3D simulation would potentially be costly. In 3D the TFSF boundary is six-sided (as depicted in Fig. 12). There are four field components per face. If the incident field is non-zero over a large number of time steps, the memory required to store the incident field could easily exceed the memory required to store the fields within the grid itself. Therefore it is envisioned that a general 3D implementation using the AFP technique would store the precomputed field to disk (possibly stored in six separate files representing the six faces). In this case, in order to make the necessary corrections to the field tangential to the TFSF boundary, a 3D FDTD simulation would merely read the stored incident field from disk. This shifts the calculation burden to an *a priori* step and the memory burden to disk. (Versions of the authors' 2D programs allow the incident field to be precomputed, stored to disk, and then read concurrently with the FDTD simulation.)

The implementation of the general 3D problem is the subject of on-going research. However, for 3D problems in which the incident field propagates orthogonal to one of the grid axes, there is a relatively simple way to implement the AFP TFSF technique efficiently. The approach is illustrated in Fig. 12. Here it is assumed that the incident field is propagating obliquely to the x and y directions, but orthogonal to the z direction (one can easily permute the indices for propagation in other direction). The polarization of the incident field is arbitrary, i.e., all six field components are allowed to be nonzero. Two 2D auxiliary simulations are performed to calculate the incident field, one for the TE^z components of the incident field and one for the TM^z components. These

simulations require that the incident field be specified over eight one-dimensional boundaries (four for each of the 2D simulations).

It is required that the TF regions of the 2D simulations be at least as big as the cross-sectional area of the TF region in the 3D grid (with the geometry shown here, this would correspond to the area of the TF region seen along a constant z plane). The auxiliary simulations do not include any scatterers. Since the fields leaked into the SF region by the AFP technique are typically so small, one need not pay much attention to termination of these auxiliary grids (i.e., since the leaked fields are often on the order of 10^{-9} one does not have to worry about using ABC's to terminate the grids). Note that the assumed locations of the interfaces shown in Fig. 9 and 10 are consistent with slices through a 3D grid.

Referring to the geometry shown in Fig. 12, the interior of the TF regions of the auxiliary grids would provide the x and y components of the fields needed at the "top" and "bottom" of the TFSF boundary in the 3D grid (i.e., at the two constant z planes). The fields on the constant x and y planes are also taken from the auxiliary simulations, but in this case, since there is no variation in the z direction, the value is only a function of x or y (the same value pertains to the entire vertical extent of the face of the boundary).

In the FDTD grid the decomposition of the incident field into TE and TM components is not trivial since, in general, the electric field, magnetic field, and direction of propagation do not form an orthogonal set. One can specify the direction of travel and the orientation of the electric field, but then one cannot use a simple vector projection of the field components and characteristic impedance of the continuous-world medium to find the relative amplitudes of the TE and TM fields. Instead, one must use the FDTD impedance relationship to determine the amplitudes. Details concerning polarization can be found in [5].

10   Conclusion

The AFP TFSF method can be readily applied to problems involving planar interfaces, whether dielectric or PEC. The method is ideally suited to oblique incidence and does not suffer the inherent approximations associated with using an auxiliary grid. If no wavenumber components are discarded from the transforms, the only errors associated with the technique would be those associated with implementation of the discrete-time Fourier transform. In practice, even when discarding superluminal wavenumber components and using a coarsely discretize incoming field, the leaked fields are approximately 100 dB down from the peak excitation. Using a discretization which is more typical of actual practice, the leaked fields are approximately 180 dB down. Modularized programs, written in C, which implement the AFP TFSF method for all the cases considered here are available from the PI.

The approach used here is not restricted to the second-order Yee FDTD algorithm. The same steps could be followed to derive an AFP TFSF technique for any FDTD method which has a rigorous dispersion relation. Additionally, the method could be applied to multiple layers where one would have to solve for the fields in the multi-layer system as is done in the continuous world. As will be discussed in a companion paper, the method can be used with lossy media, can model incident angles beyond the critical angle (i.e., where the fields in the second medium are evanescent),

and can be implemented efficiently in three dimensions.

For problems which can be solved both by the AFP technique and the traditional one-dimensional auxiliary-grid approach, the AFP technique yields far greater accuracy (except in the case of grid-aligned propagation). Furthermore, the AFP TFSF technique provides the ability to study many problems which cannot be solved using the traditional one-dimensional auxiliary-grid approach. For incident angles beyond the critical angle, the solution obtained from the AFP technique is compromised somewhat by the inherent nature of the field which arrives in advance of the in-coming wave. This degradation is unavoidable given the seemingly acausal incident field and it is believed that no other TFSF method could provide better fidelity. The AFP technique can be applied efficiently to 3D problems in which propagation is orthogonal to one of the axes. For elec-tromagnetics, this requires that two auxiliary 2D simulations be performed—only one would be required in an acoustic simulation. A general 3D implementation appears possible but this awaits the derivation of the FDTD reflection and transmission coefficients in 3D.

References

[1] D. E. Merewether, R. Fisher, and F. W. Smith. On implementing a numeric Huygen's source scheme in a finite difference program to illuminate scattering bodies. *IEEE Transactions on Nuclear Science*, 27(6):1829–1833, December 1980.

[2] A. Taflove and S. Hagness. *Computational Electrodynamics: The Finite-Difference Time-Domain Method, 3 ed.* Artech House, Boston, MA, 2005.

[3] C. Guiffaut and K. Mahdjoubi. Perfect wideband plane wave injector for FDTD method. In *IEEE Antennas and Propagat. Soc. Int. Symposium*, volume 1, pages 236–239, Salt Lake City, UT, July 2000.

[4] C. D. Moss, F. L. Teixeira, and J. A. Kong. Analysis and compensation of numerical disper-sion in the FDTD method for layered, anisotropic media. *IEEE Transactions on Antennas and Propagation*, 50(9):1174–1184, September 2002.

[5] J. B. Schneider. Plane waves in FDTD simulations and a nearly perfect total-field/scattered-field boundary. *IEEE Transactions on Antennas and Propagation*, 52(12):3280–3287, De-cember 2004.

[6] M. Celuch-Marcysiak and W. K. Gwarek. On the nature of solutions produced by finite dif-ference schemes in time domain. *International Journal of Numerical Modelling: Electronic Networks, Devices and Fields*, 12(1–2):23–40, January–April 1999.

[7] J. B. Schneider and R. J. Kruhlak. Plane waves and planar boundaries in FDTD simulations. In *IEEE Antennas and Propagat. Soc. Int. Symposium and URSI Radio Sci. Meeting*, Salt Lake City, UT, July 2000.

[8] A. V. Oppenheim, A. S. Willsky, and I. T. Young. *Signals and Systems*. Prentice-Hall, Englewood Cliffs, NJ, 1983.

[9] J. B. Schneider and C. L. Wagner. FDTD dispersion revisited: Faster-than-light propagation. *IEEE Microwave Guided Wave Letters*, 9(2):54–56, February 1999.

[10] W. Ma, M. R. Rayner, and C. G. Parini. Discrete Green's function formulation of the FDTD method and its application in antenna modeling. *IEEE Transactions on Antennas and Propagation*, 53(1):339–346, January 2005.

[11] L. N. Trefethen. Group velocity in finite difference schemes. *SIAM Review*, 24(2):113–135, 1982.

[12] D. H. Choi and J. E. Roy. The dispersion characteristics of the FD-TD method. In *IEEE Antennas and Propagat. Soc. Int. Symp.*, pages 26–29, San Jose, CA, 1989.

[13] J. B. Schneider and R. J. Kruhlak. Dispersion of homogeneous and inhomogeneous waves in the Yee finite-difference time-domain grid. *IEEE Transactions on Microwave Theory and Techniques*, 49(2):280–287, February 2001.

[14] V. Anantha and A. Taflove. Efficient modeling of infinite scatterers using a generalized total-field/scattered-field FDTD boundary partially embedded within PML. *IEEE Transactions on Antennas and Propagation*, 50(10):1337–1349, October 2002.

[15] J.-H. Chang and A. Taflove. Three-dimensional diffraction by infinite conducting and dielectric wedges using a generalized total-field/scattered-field FDTD formulation. *IEEE Transactions on Antennas and Propagation*, 53(4):1444–1454, April 2005.

[16] F. D. Hastings, J. B. Schneider, and S. L. Broschat. A Monte-Carlo FDTD technique for rough surface scattering. *IEEE Transactions on Antennas and Propagation*, 43(11):1183–1191, November 1995.

[17] E. I. Thorsos. The validity of the Kirchhoff approximation for rough surface scattering using a Gaussian roughness spectrum. *J. Acoust. Soc. Am.*, 83(1):78–92, 1988.

[18] Z. Wu and J. Fang. High-performance PML algorithms. *IEEE Microwave Guided Wave Letters*, 6(9):335–337, September 1996.

[19] W. C. Chew and J. M. Jin. Perfectly matched layers in the discretized space: An analysis and optimization. *Electromagnetics*, 16(4):325–340, 1996.

[20] J. Fang and Z. Wu. Closed-form expression of numerical reflection coefficient at PML interfaces and optimization of PML performance. *IEEE Microwave Guided Wave Letters*, 6(9):332–334, September 1996.

[21] J.-P. Bérenger. Evanescent waves in PML's: Origin of the numerical reflection in wave-structure interaction problems. *IEEE Transactions on Antennas and Propagation*, 47(10):1497–1503, October 1999.

[22] J. A. Pereda, O. García, A. Vegas, and A. Prieto. Numerical dispersion and stability analysis of the FDTD technique in lossy dielectrics. *IEEE Microwave Guided Wave Letters*, 8(7):245–247, July 1998.

[23] G. Sun and C. W. Trueman. Numerical dispersion and numerical loss in explicit finite-difference time-domain methods in lossy media. *IEEE Transactions on Antennas and Propagation*, 53(11):3684–3690, 2005.

[24] V. L. Brudny and W. L. Mochán. On the apparent superluminality of evanescent waves. *Optics Express*, 9(11):561–566, 2001.

[25] V. L. Brudny and W. L. Mochán. FTIR and the illusion of superluminality. In *2004 OSA Annual Meeting*, Rochester, NY, October 2004.